

## **A model of the near magnetosphere with a dawn-dusk asymmetry**

### **2. Parameterization and fitting to observations**

N. A. Tsyganenko

Universities Space Research Association and Laboratory for Extraterrestrial Physics, NASA Goddard Space

Flight Center, Greenbelt, Maryland

Short title: A NEW MAGNETOSPHERE MAGNETIC FIELD MODEL

**Abstract.** First results are presented of an empirical modeling of the Earth's inner and near magnetosphere ( $X \geq -15 R_E$ ), using a new set of data and new methods, described in a companion paper. The modeling database included 5-min average B-field data, taken in a wide range of altitudes and latitudes by the ISTP spacecraft Polar (1996-99) and Geotail (1994-99), as well as by earlier missions ISEE-2 (1984-87), AMPTE/CCE (1984-88), AMPTE/IRM (1984-86), CRRES (1990-91), and DE-1 (1984-90). To take into account the delayed response of the magnetosphere to the solar wind and interplanetary magnetic field (IMF), each data record in the dataset was tagged by a "trail" of 5-min averages of the IMF, solar wind, and  $Dst$ -field data, covering the preceding 2-hour interval. The axisymmetric ring current (SRC) and the partial one (PRC), both parameterized by the corrected  $Dst^*$  index and the solar wind pressure  $P_d$ , were found to vary in strikingly different ways. While under quiet conditions the PRC is much weaker than the SRC, it dramatically grows in magnitude and rotates to the dusk sector with rising  $|Dst^*|$  and  $P_d$ , significantly exceeding the SRC even during moderate storms, in excellent agreement with recent particle simulations. The innermost part of the cross-tail current is quite sensitive to the southward IMF and yields  $\sim 90\%$  of the tail's contribution to the  $Dst$  index, in contrast with the more distant tail current, which responds mainly to the solar wind pressure and provides no appreciable contribution to  $Dst$ . In response to southward IMF conditions, Region 1 and 2 Birkeland currents rapidly grow in magnitude and expand to lower latitudes, while their peaks shift slightly in local time towards noon. The coefficient of the IMF penetration inside the magnetosphere was found to dramatically increase with growing IMF clock angle: while quite small ( $\sim 0.1$ ) for northward IMF, it rises to  $\sim 0.6$  as the IMF turns southward. Priorities and challenges for future data-based modeling studies are discussed.

## 1. Introduction

In the companion paper [Tsyganenko, 2001], hereafter called Paper 1, a new model of the magnetic field in the near magnetosphere ( $X \geq -15 R_E$ ) was presented. That work concentrated on a detailed description of mathematical elements of the model, each representing a contribution to the total field from a major magnetospheric electric current system. This paper presents first results of fitting that model to a new set of space magnetometer data, mostly from two ISTP spacecraft, Polar and Geotail, complemented by lesser amounts of data from earlier missions ISEE-2, AMPTE/CCE/IRM, CRRES, and DE-1. The data are described in section 2, followed by a detailed account on how the parameters of the model field sources depend on the concurrent state of the solar wind and the ground disturbance level (section 3). Section 4 addresses the derivation of the model field from the data and presents some results of testing the new model; it is followed by a discussion of principal findings in section 5, and a brief summary.

## 2. Data Set

Space magnetometer data, complemented by the concurrent solar wind and ground-based observations, are one of the essential "pillars" of the empirical modeling. Over the past three decades, a vast amount of such data was collected by many spacecraft at different locations, seasons, solar cycle stages, and disturbance levels. *Mead and Fairfield* [1975] compiled the first set of distant magnetospheric field data, taken by four IMP spacecraft during 1966-1972, and used it to create an empirical model, binned by Kp-index. *Tsyganenko and Usmanov* [1982] added HEOS-1 and -2 data to the set of Mead and Fairfield and developed a more realistic model with an explicitly defined ring current and a tail current sheet. The dataset was further extended by Tsyganenko and Malkov [see *Peredo et al.*, 1993] who added ISEE-1/2 data from 1977-1981, while Fairfield independently added HEOS observations and additional IMP-6 data to the original Mead-Fairfield database. Editing those data and merging them into one large database resulted in a set covering the period from 1966 to 1986 and described by *Fairfield et al.* [1994]. It was used in the derivation of the T96 global field model, which not only represented average static configurations, but also revealed the response of individual field sources to changes in the external conditions.

As large as that dataset was, it became clear that much more data were needed, covering the full range of all variables - not only the  $\{X,Y,Z\}$  coordinates, but also the added dimensions of the geodipole tilt angle, the geomagnetic activity level (e.g., *Dst*-index), solar wind pressure, and IMF components. In this respect, the dataset of Fairfield et al. still had many gaps. In particular, most of the data came from quiet and moderately disturbed periods, while unusual conditions in the solar wind (most important for the space weather) were significantly underrepresented. New observations during the last decade filled numerous gaps in the coverage. The Geotail spacecraft provided excellent mapping of the tail plasma sheet, especially in its near-Earth part, where the most interesting space weather phenomena take place. The Polar spacecraft with its highly inclined orbit greatly improved the sampling at high latitudes, including the polar cusps and the very important region of Birkeland currents. Last but not least, the data of Wind provided a continuous coverage of the state of the interplanetary medium, making it possible to tag the magnetospheric data records with "trails" of solar wind parameters for the preceding 2-hour intervals. That opened a possibility of modeling the effects of a delayed response of the magnetosphere to changing external conditions.

In this modeling effort, a uniform 5-min resolution was adopted for all magnetospheric and concurrent solar-wind/ground-based data, including the new SYM/ASY *Dst*-field. The 5-min time interval corresponds to a  $\sim 20 R_E$  travel distance of the solar wind flow around the magnetosphere, commensurate with its transverse scale size. It therefore can be assumed as a minimal time scale for the magnetosphere to respond to changes in the external pressure. A finer resolution would lead to unreasonably large and redundant datasets, while longer intervals could miss short-term variations due to transient gusts of the solar wind. In this regard it is also important to note that the rate of the field reconfiguration owing to dayside merging can be quite fast. Low-altitude data [Newell et al., 1997] have shown that even transient periods of 4-10 min of southward IMF  $B_z$ , embedded in a long interval of northward  $B_z$ , can dramatically affect the size of the polar cap and hence the global magnetospheric structure.

A perfect solution would be to merge together old and new data, in order to maximize the coverage, both in the geometrical and in the parametrical space. However, the old data set has some limitations that for now preclude us from unifying it with the new one. In particular, the temporal resolution of the old data for the

magnetospheric field was between 10 minutes and 1 hour, while the concurrent solar wind parameters, IMF, and *Dst*-index (all from the OMNI database) were represented by hourly averages. Even though it was in principle possible to recover shorter time variations by reprocessing at least a part of the original magnetospheric data, the high-resolution *Dst* (SYM) index was unavailable for years before 1984, and therefore this is where the newly created dataset begins.

In the new dataset, the temporal coverage of the entire period 1984-1999 is still rather non-uniform, mainly because of many gaps in the interplanetary data before the launch of Wind. Figure 1 displays the distribution of data with time and by spacecraft; its format is similar to that of Figure 3 of *Fairfield et al.* [1994]. To better visualize relative amounts of data from different spacecraft, the thicknesses of the corresponding horizontal bars were made proportional to the square root of the numbers of data records per one year. More details on the data from individual spacecraft are given in the following sections.

## 2.1. Magnetospheric Magnetic Field Data

Magnetospheric data were provided by the following 7 spacecraft: Geotail, Polar, ISEE-2, AMPTE/CCE, AMPTE/IRM, CRRES, and DE-1. Typical basic procedures involved in the data processing were (1) initial retrieval, (2) reformatting, (3) merging with the concurrent solar wind data, (4) selection of data taken inside the model magnetopause (whose size and shape were defined using the concurrent solar wind conditions), (5) subtraction of the internal field, evaluated by an appropriate IGRF model, (6) a visual inspection of the data plots and their comparison with an expected model field (T96), with the goal of eliminating bad data records, (7) averaging over 5-min intervals, and (8) tagging the magnetospheric data records with 2-hour trails of the solar wind and *Dst* (SYM) data (records with incomplete trails were left out).

**2.1.1. Geotail data.** Geotail magnetometer data in the new dataset covered the 5-year period from November 1994 to November 1999, when the spacecraft was transferred into the near-tail phase of its operation at distances between 10 and 30  $R_E$ . Owing to the low inclination of the Geotail orbit, most data were taken either inside the plasma sheet or not far from it in the tail lobes. More details on the Geotail orbit and its magnetometer experiment can be found elsewhere [Nishida, 1994; Kokubun *et al.*, 1994].

An important part of the Geotail data processing was the elimination of an offset in the  $B_z$  component measured in the spacecraft coordinate system, reported by the Geotail magnetometer team [S. Kokubun, T. Mukai, private communication, 1997-1999]. Owing to its small magnitude and transverse orientation with respect to Sun-Earth line, the offset had no substantial effect on the tail lobe field and, hence, it did not affect the results of our previous studies of the shape of the cross-tail current [Tsyganenko *et al.*, 1998] and of the tail lobe field [Tsyganenko, 2000a]. However, it must be taken into account in the plasma sheet data, because the total field there drops down to only a few nanotesla.

Since the Z-axis in the spacecraft coordinate system is nearly perpendicular to the ecliptic plane, and the absolute values of the offset  $\Delta B_z$  did not exceed 1 nT, the correction was actually made in GSE coordinates. Using a monthly table of offsets (courtesy T. Nagai, ISAS), a smooth approximation was derived for  $\Delta B_z$  as a superposition of separate piece-wise Fourier expansions for each yearly interval. Figure 2 shows the offset as a function of time, with the crosses representing the tabular data and the solid line derived from the analytical approximation used in the correction procedure.

Figure 3 shows the spatial distribution of Geotail data, included in the final modeling dataset. Note the excellent coverage of the near magnetotail at low GSM latitudes. The total number of Geotail data records with 2-hour solar wind data trails was 9,573.

**2.1.2. Data of Polar.** The Polar Magnetic Field Experiment (MFE) provided abundant data in the high-latitude magnetosphere, only poorly covered by previous missions, in a wide range of distances up to  $8.8 R_E$ . More details on the orbit of Polar and on the MFE were given by Russell *et al.* [1995]. The original 1-min average data from the UCLA Polar website were processed in nearly the same way as the Geotail data, described in the previous section, but using a more sophisticated magnetopause model with an indentation in the vicinity of the polar cusp [Tsyganenko, 2000b]. That was done to remove ambiguous data of possible magnetosheath origin, in order to ensure a clean magnetospheric data set. The data covered the period from March 1996 to August 1999 and contributed the largest number of records in the final database: 28,351. Figure 4 shows the coverage by the Polar data in a format similar to that of Figure 3.

**2.1.3. ISEE-2 data.** The ISEE-2 satellite was launched in October 1978 into a highly eccentric orbit with an inclination  $28.77^\circ$  and an apogee of  $23 R_E$ . More details on the orbit were given by *Ogilvie et al.* [1977], and the magnetic field experiment was described by *Russell* [1978]. Unlike Geotail, ISEE-2 covered a wider range of latitudes; however, because of the lack of high-resolution *Dst* data, only the data for 1984-1987 were included in the modeling set. During that period, IMP 8 was the sole monitor of the interplanetary medium, and its solar wind and IMF coverage had many gaps. For that reason, ISEE-2 provided only 1224 records to the set; their spatial distribution is shown in Figure 5.

**2.1.4. AMPTE/CCE data.** The AMPTE/CCE spacecraft was launched on August 16, 1984, with an orbital period of 15.7 hours, an inclination of  $4.8^\circ$ , and an apogee of  $8.8 R_E$ . A detailed description of its orbit and of the magnetic field experiment were given by *Bryant et al.* [1985] and *Potemra et al.* [1985], respectively. Since AMPTE/CCE was not a magnetically clean spacecraft, it was important to minimize possible contamination fields in the data. An intercomparison with simultaneous AMPTE/IRM and AMPTE/UKS magnetometer data made it possible to derive the correction to the axial component of the field, which was found equal to 12.9 nT [Fairfield et al., 1987]. Data used in this study were obtained from NSSDC tapes as 68-sec average magnetic field vectors. The concurrent position vectors were calculated by means of a cubic interpolation, using consecutive 5-min values of ephemeris elements from separate files. Otherwise, the data processing included the same steps as those listed in the beginning of section 2.1. The data covered the interval 1984-1988, though most of them by far came from the last three years of spacecraft operation (1986-1988). Figure 6 displays the spatial distribution of the AMPTE/CCE data in our data set. As in the case of Polar, this spacecraft spent most of its time inside the magnetosphere; however, in contrast with Polar, AMPTE/CCE provided only 2982 data records (about one-tenth of Polar's contribution), because of the already mentioned scarcity of continuous solar wind data in the 1980s.

**2.1.5. AMPTE/IRM data.** The AMPTE/IRM spacecraft was launched on August 16, 1984, into an elliptical orbit with an inclination of  $28.6^\circ$  and an apogee of  $18.83 R_E$ . Like ISEE 2, it passed through the nightside magnetosphere during the spring months, but the apogees of AMPTE/IRM were located at much lower solar ecliptic latitudes (and to the south of the ecliptic plane). More details on the orbit were given by *Bryant et al.* [1985]; the same publication contains a description of the magnetometer experiment [Luhr et al., 1985].

The original 4-s average magnetometer data underwent an initial crude selection and averaging over 1-min intervals. After that, the data were processed using the same basic procedures. AMPTE/IRM provided the smallest contribution to the dataset: only 210 records with 2-hour solar wind data trails. Their spatial distribution is included in Figure 5 together with the ISEE-2 data points.

**2.1.6. CRRES data.** The CRRES spacecraft was launched on July 25, 1990, with the initial orbital period 9 hours 52 min, inclination of  $18.2^\circ$ , perigee of 350 km, and apogee  $6.3 R_E$ . Its data covered the inner magnetosphere for a nearly 13-month period, until the failure of the spacecraft in September 1991. The magnetometer experiment onboard CRRES was described in detail by *Singer et al.* [1992]. In the present work, only the high-gain data with  $B < 850$  nT were used. The low-gain data, taken at  $R < 3.5 R_E$  were left out because of their generally lower accuracy (H. Singer, private communication, 1994, 1999). The data taken during spacecraft eclipses and within 30 min thereafter were also left out, because of large-amplitude field oscillations of clearly artificial origin, typically observed during such events. The total number of data records contributed by CRRES to our set was 563; Figure 7 displays their spatial distribution.

**2.1.7. DE-1 data.** The DE-1 spacecraft was launched on August 3, 1981 into an elliptical orbit with the period 6 hours 50 min, inclination  $88.8^\circ$ , perigee 468 km, and apogee  $3.66 R_E$ . Owing to a significant apsidal precession rate, the spacecraft provided a fairly uniform coverage of the inner magnetosphere, at all local times, both at high and low latitudes. The data spanned almost 9 years from 1981 to 1990. A detailed description of the spatial coverage by DE-1 was made by *Nakabe et al.* [1997], who carried out a statistical study of the inner magnetospheric magnetic field.

The DE-1 magnetometer instrument was described by *Farthing et al.* [1981]. The data used in this work were obtained from the NSSDC as 6-second averages and, after an initial transformation from geodetic to GSM coordinates and subtraction of the Earth's internal field, the dataset was divided into several bins of the radial geocentric distance. A comparison of the measured field with that given by an IGRF model revealed many cases of unrealistically large discrepancies, which could not be related to any external field sources. Most of such cases were observed inside  $R = 3 R_E$ , and therefore we eventually decided to use only the data taken at  $R > 3 R_E$ . After an intermediate averaging to 1-min resolution, the data were tagged by concurrent *Dst* and solar wind



data, after which a visual inspection was made of the scatter plots of the observed field against that predicted by the T96 model, and ambiguous data points were removed. Finally, the 1-min data were reduced to 5-min resolution. Since the spacecraft speed at  $R = 3 R_E$  was  $\sim 0.03 R_E/\text{min}$ , the 5-min averages corresponded to the spatial resolution of  $\sim 0.15 R_E$ . The total number of the DE-1 data records in the set was 2299, and their spatial coverage is shown in Figure 8.

## 2.2. Solar Wind Data

This work used 5-min averaged solar wind and IMF data, compiled from higher-resolution data of IMP 8 and Wind spacecraft. The IMP 8 solar wind plasma data were derived from 1-min averages, provided by the MIT Space Plasma Group website, while the IMF data were calculated from 15-s averages, retrieved from the NSSDC online database. The Wind data were obtained from the NSSDC website with 1-min resolution and were subsequently averaged over 5-min intervals.

In order to minimize possible contamination of the IMP 8 data by measurements made in the magnetosheath, only the data taken at positive  $X_{\text{GSM}}$  were selected. A constraint was also imposed on the Wind data, leaving out the measurements made on solar wind streamlines which passed farther than  $\rho = 40 R_E$  from the Earth's center. The streamline orientations were determined from the measured components of the solar wind bulk flow velocity at the Wind location and extrapolated from there to Earth's orbit. There is a strong evidence [e.g., *Richardson and Paularena*, 2001, and references therein] that the distance  $\rho$  is critical for the accuracy of estimating the solar wind parameters in front of the magnetosphere using the upstream data taken at the L1 point.

The original data also contained a small percentage of isolated records with abnormally high density ( $N > 50 \text{ cm}^{-3}$ ) or with unrealistically large spikes of the IMF. Such suspicious records were visually checked and deleted. To take into account the finite travel time of the solar wind from the upstream location of the monitoring spacecraft, observation times for all the data were reduced to the Earth's location by introducing an appropriate time lag, based on the current position of the spacecraft and the measured flow velocity. When both Wind and IMP 8 data were available for a given 5-min interval, the IMP 8 data records were preferred, since most Wind measurements were made at much larger upstream distances and hence could result in larger errors. More

details on the solar wind data preparation can be found in our earlier paper [Tsyganenko *et al.*, 1999].

### 2.3. Ground Based Data

The magnetospheric sources provide a significant contribution to the geomagnetic variations on the ground. For that reason, the routinely monitored *Dst*-field can provide important additional information on these sources (especially, pertaining to the ring and tail currents), complementing the space magnetometer data. Although the standard hourly *Dst*-index is not a perfect indicator of the magnetospheric state [Campbell, 1996], it was used as an input parameter in the models of Hilmer and Voigt [1995], Ostapenko and Maltsev [1998], and in the T96 model. One of general goals of the present effort is to "animate" the data-based models by enabling them to reproduce the continuous magnetospheric response to changing solar wind conditions. For that reason, it was decided to replace the hourly *Dst*-index by the higher-resolution longitudinally symmetric (SYM) index by Iyemori [1990], which has also been used in our previous studies of the inner magnetosphere [Tsyganenko *et al.*, 1999] and the tail lobe field [Tsyganenko, 2000a].

As already mentioned, the SYM index was available only since 1984, which is one of the reasons why the present dataset did not include earlier spacecraft data. Since the original SYM index had 1-min resolution, it was averaged over 5-min intervals, to match the magnetospheric and solar wind data, and these averages were included in the corresponding records of the modeling data set. Keeping in mind future modeling studies of magnetospheric storms, each record was also provided with "trailing" values of the SYM-index for the preceding 2-hour interval.

## 3. Parameterization of the Model

In parameterizing a model, we seek an optimal functional relation between the strength of the magnetospheric field sources and the state of the interplanetary medium and/or indices, routinely monitored at the ground. In early models [Mead and Fairfield, 1975; Tsyganenko and Usmanov, 1982; Tsyganenko, 1987, 1989], the entire data set was divided into several subsets, corresponding to different intervals of the Kp-index, and separate sets of the model coefficients were found for each bin of Kp. In the case of more than one input parameter, this

simple method becomes unfeasible due to the rapidly growing number of bins, each of which contains too few data points.

In the T96 model, a more sophisticated approach was used: the input parameters (solar wind ram pressure  $P_d$ ,  $Dst$ -index,  $B_y$  and  $B_z$  components of the IMF) entered the model's field coefficients as continuous variables and were treated in the same way as the spatial coordinates  $\{X, Y, Z\}$  and the dipole tilt angle  $\Psi$ . In other words, the components of the model field were considered as functions of a vector with 8 components,  $\{X, Y, Z, \Psi, P_d, Dst, B_y^{IMF}, B_z^{IMF}\}$ , which allowed us to avoid binning and instead fit the model to the entire data set.

However, even though that method was a major step forward, it method left much room for improvement. In the T96 model, the amplitudes of the individual field sources were assumed to depend only on current values of the external parameters, which tacitly implied that the model's response to the external input did not depend on previous conditions. In actuality, a magnetospheric configuration depends not only on the present state of the solar wind, but also on its pre-history for at least a few preceding hours. This is especially true for the inner magnetosphere, since its condition is largely governed by plasma convection from the tail, which may take from at least tens of minutes up to an hour or even longer. In the present work, an attempt is made to take into account these effects, using the new data set with higher temporal resolution.

### 3.1. Parameterizing the tail field terms

The fringe field of the cross-tail current contributes significantly to the field in the inner and near magnetosphere, and in recent years its dependence on the solar wind parameters has been extensively studied. In particular, it was found that, because of the decreasing magnetopause flaring angle, the tail lobe field  $B_L$  becomes significantly less sensitive to the solar wind ram pressure  $P_d$  when that is large. As a result, its dependence is better described either by a power law  $B_L \sim P_d^{1/4}$  [Fairfield and Jones, 1996] or even by a logarithmic one  $B_L \sim \ln P_d$  [Tsyganenko, 2000a]. In the latter work, we also tried other IMF-related regression terms, and the best results for the near-tail lobe field were obtained with the one resembling the solar wind energy transfer function  $\epsilon = V B_{\perp}^2 \sin^4(\theta/2)$  [Akasofu, 1979], with  $V$ ,  $B_{\perp}$ , and  $\theta$  being the solar wind speed, the IMF transverse

component, and its clock angle, respectively. More specifically, the highest multiple correlation coefficient of the model tail lobe field with data was found when using the regression term

$$G_1 = \langle V h(B_\perp) \sin^3 \frac{\theta}{2} \rangle = \sum_{i=1}^{12} W_i V_i h(B_{\perp_i}) \sin^3 \frac{\theta_i}{2}, \quad (1)$$

where the function  $h(B_\perp) = (B_\perp/40)^2/(1+B_\perp/40)$  [Tsyganenko, 2000a, Eq.(8)] behaves as  $\sim B_\perp^2 = B_y^2 + B_z^2$  for commonly observed values of the IMF, but gradually transforms into a linear dependence on  $B_\perp$  for  $B_\perp \geq 40 \text{ nT}$ . The averaging in (1) was made over the one-hour interval preceding the current observation of the magnetospheric field, with a set of weight coefficients  $W_i$  for the 12 preceding 5-min intervals. The  $Dst$  term was also found to play a significant role in the nearest bin of the tailward distance ( $10\text{--}15R_E$ ), but its contribution rapidly decreased at larger distances.

With the above results in mind, the following forms were adopted here for the amplitude coefficients  $t_1$ , and  $t_2$  (mnemonically,  $t$  stands for "tail") defining the contributions to the model field from the two tail modules, described in detail in Paper 1:

$$\begin{aligned} t_1 &= t_1^{(0)} + t_1^{(1)} (P_d/P_{d0})^{\alpha_1} + t_1^{(2)} G_1 + t_1^{(3)} Dst^* \\ t_2 &= t_2^{(0)} + t_2^{(1)} (P_d/P_{d0})^{\alpha_2} + t_2^{(2)} G_1 + t_2^{(3)} Dst^* \end{aligned} \quad (2)$$

where the first and second equations are for the short and long tail modules, respectively. The average solar wind ram pressure  $P_{d0}$  in (2) was assumed equal to 2 nPa. The power indices  $\alpha_1$  and  $\alpha_2$  were treated as free model parameters, defining, respectively, the response of the inner and more distant tail field to variations of the solar wind ram pressure. Although the new dataset made it in principle possible to take into account solar wind conditions during two-hour periods, preceding each magnetospheric observation, in the present work we used only the data for the preceding one-hour intervals. A uniform time averaging was assumed in the IMF-related function  $G_1$ , with all the weight coefficients  $W_i$  equal to 1/12; a more detailed study using an optimal linear filtering technique and longer (two-hour) data trails is planned for a future work. The asterisk in  $Dst^*$  identifies it as the corrected  $Dst$ -index, in which the Earth's induction field and the field of magnetopause currents were taken into account, so that  $Dst^*$  corresponds mostly to the contribution from magnetospheric sources. The correction was made using an approximate formula  $Dst^* = 0.8 Dst - 13\sqrt{P_d}$ , similar to the one adopted in the T96 model.

To take into account possible earthward/tailward shift of the tail current, an additional degree of freedom was introduced, a variable shift  $\Delta X$  of the inner edge of the current sheet. It was represented as a linear function

$$\Delta X = \Delta X_0 + \Delta X_1 G_2 \quad (3)$$

of a parameter

$$G_2 = a \langle V B_s \rangle = a \sum_{i=1}^{12} W_i V_i B_{s_i} , \quad (4)$$

where  $V$  and  $B_s$  are the solar wind speed and the southward component of the IMF ( $B_s = |B_z|$  for  $B_z < 0$  and  $B_s = 0$  for  $B_z > 0$ ), respectively; the angular brackets denote averaging over the preceding 1-hour interval.

The constant factor  $a = 0.005$  was introduced just for convenience, to keep the parameter  $G_2$  within the range  $0 \leq G_2 \leq 10$ , for commonly observed values of  $V$  and  $B_s$ . For example, for steady interplanetary conditions with  $V = 400$  km/s,  $B_y = 0$ , and  $B_z = -5$  nT, the parameters  $G_1$  and  $G_2$  equal  $\approx 6$  and 10, respectively. The relation (3) is just one of many possible choices, based on a simple assumption that variations of the convection electric field, associated with the southward IMF, should result in a proportional shift of the inner edge of the current sheet.

### 3.2. Parameterizing the ring current

In our initial experiments, the amplitudes  $s$  of the symmetric and  $p$  of the partial components of the ring current were represented as linear functions of the corrected SYM-index  $Dst^*$ . Later on, an additional term proportional to  $\sqrt{P_d}$  was introduced, in order to allow more freedom for the corresponding correction coefficient of the  $Dst$ -field. That resulted in the following parametric dependence:

$$\begin{aligned} s &= s^{(0)} + s^{(1)} Dst^* + s^{(2)} \sqrt{P_d} \\ p &= p^{(0)} + p^{(1)} Dst^* + p^{(2)} \sqrt{P_d} \end{aligned} \quad (5)$$

The spatial scaling factors for the symmetrical ring current (SRC) and the partial one (PRC), defined in section 2.1 of Paper 1, were adopted from the following considerations. In a crude approximation by a circular current loop of a radius  $R$ , the magnetic moment of the ring current is  $M \sim B_0 R^3$ , where  $B_0$  is the disturbance at the center of the loop (roughly proportional to  $Dst^*$  in our case). Hence,  $R \sim (M/B_0)^{1/3}$ , which prompts the

scaling of both components of the ring current by power functions of  $Dst^*$ :

$$\begin{aligned}\xi_s &= \xi_{s0} \left[ \frac{20}{\max\{20, |Dst^*|\}} \right]^{\beta_s} \\ \xi_p &= \xi_{p0} \left[ \frac{20}{\max\{20, |Dst^*|\}} \right]^{\beta_p}\end{aligned}\quad (6)$$

Here we chose 20 nT as a threshold value of  $|Dst^*|$ , so that for a quiet ring current with  $|Dst^*| \leq 20$ , (6) yields

$\xi_s = \xi_{s0}$  and  $\xi_p = \xi_{p0}$ , while for stronger magnitudes of the ring current, its size becomes dependent on  $Dst^*$ .

In this approximation,  $\beta_s = 1/3$  yields a nearly constant value of the magnetic moment of the SRC, regardless of its intensity, while the cases  $\beta_s < 1/3$  ( $\beta_s > 1/3$ ) correspond to an increase (decrease) of the magnetic moment with growing  $Dst^*$ .

As already discussed in Paper 1, another important characteristic of the partial ring current is the rotation angle  $\delta$  of its peak from midnight towards dusk. A simple parametric dependence of that angle on  $Dst^*$

$$\delta = \frac{\pi}{2} \tanh \frac{|Dst^*|}{Dst_0^*} \quad (7)$$

was assumed, yielding a small duskward rotation for quiet conditions and nearly  $90^\circ$  rotation for strong storms.

The parameter  $Dst_0^*$  in (7) is a characteristic threshold value of  $Dst^*$ , defining the sensitivity of the angle  $\delta$  to the disturbance level.

The quantities  $\xi_{s0}$ ,  $\xi_{p0}$ ,  $\beta_s$ ,  $\beta_p$ , and  $Dst_0^*$  were all considered free nonlinear parameters of the model ring current, to be determined from the least-squares fitting to the data. The results of their calculations will be discussed in section 4.2 below.

### 3.3. Parameterizing Birkeland currents

It is well established that Region 1 Birkeland currents serve as a principal link between the interplanetary medium and the ionosphere, electrostatically transferring the momentum from the solar wind flow and thereby stirring up the anti-sunward ionospheric convection at high latitudes. However, many questions remain unanswered so far; in particular, it is still unclear which combination of the solar wind parameters is the best predictor of the total strength of the Region 1 currents. That problem was addressed by *Iijima and Potemra* [1982] and *Bythrow and Potemra* [1983], and, no surprise, it was found that the interplanetary electric field played an important role.

This study only makes a tentative choice of the driving parameters for the Birkeland currents, reflecting two major factors responsible for magnetospheric convection: (1) a viscous drag, resulting in a relatively constant residual electric field across the polar cap, and (2) IMF reconnection, which dramatically boosts the convection in the plasma sheet during southward IMF intervals, but recedes into the background as the IMF turns northward. With these considerations, we chose the amplitudes of the Region 1 Birkeland current modes as linear functions of the parameter  $G_2$ , defined by (4) in section 3.1. Region 2 currents, located at lower latitudes, also rise and fall with magnetospheric convection, but they should be viewed as a consequence of that convection, rather than one of its causes.

Based on the above arguments, we chose a simple parameterization for the coefficients  $b_l^{(m)}$  ( $b$  for "Birkeland") defining the magnitude and longitudinal variation of both Region 1 and 2 currents:

$$b_l^{(m)} = b_l^{(m0)} + b_l^{(m1)} G_2 \quad (8)$$

where the lower index  $l = 1, 2$  refers to the Region 1 or 2 systems, respectively, and the upper one  $m = 1, 2$  corresponds to the longitudinal Fourier mode number, as defined in Eq. (17) of Paper 1.

The spatial scaling factors  $\varsigma_1$  and  $\varsigma_2$  for the Region 1 and 2 Birkeland currents, respectively, were also assumed to be simple linear forms of the IMF-related parameter  $G_2$

$$\begin{aligned} \varsigma_1 &= \varsigma_1^{(0)} + \varsigma_1^{(1)} G_2 \\ \varsigma_2 &= \varsigma_2^{(0)} + \varsigma_2^{(1)} G_2 \end{aligned} \quad (9)$$

One can expect  $\varsigma_{1,2}^{(0)} \sim 1$  and  $\varsigma_{1,2}^{(1)} > 0$ , so that the model Region 1 and 2 zones are found around their normally observed locations at quiet conditions, but shift equatorward as the IMF turns southward.

### 3.4. Parameterizing the magnetopause magnetic field

In the present approach, the magnetic field of the magnetopause currents is fully determined by the shape and size of the boundary, as well as by the strength and spatial distribution of the fields of internal magnetospheric currents. The shape and size of the magnetopause are uniquely defined in this model by the solar wind pressure  $P_d$  and the tilt angle  $\Psi$  of the geodipole, as discussed in detail in section 2.4 of Paper 1. The net magnetopause field is the sum of several terms, in which the dipole shielding field  $\mathbf{B}_{CF}$  dominates over

others; it was described in detail in section 2.4.1 of Paper 1 and was scaled in the model by the magnetosphere compression factor  $\chi$  as  $\mathbf{B}'_{\text{CF}}(\mathbf{r}) = \chi^3 \mathbf{B}_{\text{CF}}(\chi \mathbf{r})$ . The rest of the magnetopause field, shielding the contributions of magnetospheric sources, was parameterized implicitly via the amplitude coefficients and nonlinear parameters of the corresponding current systems. The only additional free parameter here was the power index  $\kappa$ , entering in the common scaling factor as  $\chi = (P_d/P_{d0})^\kappa$ . Its starting value in the fitting runs was set equal to a theoretical estimate  $\kappa = 1/6$  [e.g., *Mead and Beard*, 1964]. It is also important to note that the same uniform scaling by the solar wind pressure with the factor  $\chi$  was applied to the tail and Birkeland currents, in order to keep their fields fully shielded within the same common boundary for any value of  $P_d$ . The size of the ring current was controlled only by the corrected  $Dst^*$  entering in the scaling factors in (6), and the full confinement of the ring current field inside the magnetopause was ensured by making its shielding field depend on those factors, as detailed in section 2.4.2.2 (Eq. (34)–(35)) of Paper 1.

As already noted in Paper 1, no explicit dependence of the magnetopause shape on the IMF was assumed in this model, although IMF effects are implicitly present via the IMF-related terms, entering in the amplitudes and geometrical parameters of the shielded cross-tail and Birkeland currents. In addition, the magnetopause field receives a contribution from the IMF interconnection term, discussed in the next section. Inclusion of that term can also be viewed as expressing the effect of an IMF-induced redistribution of magnetopause currents, leading to incomplete shielding and hence, to a finite  $B_n$  on the boundary.

### 3.5. IMF interconnection field

As detailed in Paper 1 (section 2.5, Eq.(39)), the finally adopted form of the interconnection term was just a uniform magnetic field vector  $\varepsilon \mathbf{B}_\perp^{\text{IMF}}$ , collinear with the transverse component of the IMF. Initially, the attenuation factor  $\varepsilon$  was assumed constant and thus independent on the IMF orientation; later, an interesting opportunity was realized to check whether the penetration efficiency  $\varepsilon$  depended on the IMF clock angle  $\theta$ . It is well known (e.g., [*Wygant et al.*, 1983] and references therein) that the cross-polar-cap potential is a highly nonlinear “rectified” function of the interplanetary electric field, dropping to low values when the IMF clock angle is small, but rising dramatically for  $\theta \sim \pi$ . It is in principle possible that the degree of the IMF penetration



may behave in a similar way; to verify this conjecture, the factor  $\varepsilon$  was represented as

$$\varepsilon = \varepsilon_0 + \varepsilon_1 \sin^2 \frac{\theta}{2}, \quad (10)$$

and the coefficients  $\varepsilon_0$  and  $\varepsilon_1$  were treated as free model parameters.

#### 4. Derivation of the Model Field from the Data

The model field described above is the sum of five physically different vector fields, entering in Eq. (1) of Paper 1. Three of those fields (corresponding to the cross-tail current, ring current, and Birkeland currents), have been further split into sums of separate modules, so that the final form of the net external model field  $\mathbf{B}_{\text{mod}}$  reads as follows

$$\begin{aligned} \mathbf{B}_{\text{mod}} = & \mathbf{B}_{\text{CF}} + \left[ t_1^{(0)} + t_1^{(1)} (P_d/P_{d0})^{\alpha_1} + t_1^{(2)} G_1 + t_1^{(3)} Dst^* \right] \mathbf{B}_{\text{T1}} \\ & + \left[ t_2^{(0)} + t_2^{(1)} (P_d/P_{d0})^{\alpha_2} + t_2^{(2)} G_1 + t_2^{(3)} Dst^* \right] \mathbf{B}_{\text{T2}} + \left[ s^{(0)} + s^{(1)} Dst^* + s^{(2)} (P_d/P_{d0})^{1/2} \right] \mathbf{B}_{\text{SRC}} \\ & + \left[ p^{(0)} + p^{(1)} Dst^* + p^{(2)} (P_d/P_{d0})^{1/2} \right] \mathbf{B}_{\text{PRC}} + \left[ b_1^{(10)} + b_1^{(11)} G_2 \right] \mathbf{B}_{\text{R1}}^{(1)} + \left[ b_1^{(20)} + b_1^{(21)} G_2 \right] \mathbf{B}_{\text{R1}}^{(2)} \\ & + \left[ b_2^{(10)} + b_2^{(11)} G_2 \right] \mathbf{B}_{\text{R2}}^{(1)} + \left[ b_2^{(20)} + b_2^{(21)} G_2 \right] \mathbf{B}_{\text{R2}}^{(2)} + \left[ \varepsilon_0 + \varepsilon_1 \sin^2 \frac{\theta}{2} \right] \mathbf{B}_{\perp}^{\text{IMF}} \end{aligned} \quad (11)$$

In total, the field (11) includes 24 coefficients and 18 nonlinear parameters, whose values are to be found from the data. Considering the high variability of the magnetospheric and interplanetary conditions, inevitable inaccuracies of the downstream mapping of the solar wind data taken at the L1 point, possible undetected intervals of bad data, and other factors, one might wonder if all those parameters can be resolved in a meaningful way.

##### 4.1. Fitting Criterion

An important question here is what kind of a merit function should be used when fitting the model to the data. In the derivation of the T96 model, we used a "directional" criterion, optimizing the mapping accuracy. In that approach, the merit function was calculated as an rms deviation of the model field directions  $\mathbf{b} = \mathbf{B}/B$  from the observed ones. That method yielded reasonable and robust results in the regions with weak magnetic fields, such as the magnetotail. However, at closer geocentric distances the merit function based on the directional

criterion becomes progressively less and less sensitive to the external field, because of the rapid growth of the Earth's main field. In the inner magnetosphere, the geomagnetic field remains nearly quasi-dipolar at almost all times, except during strong storms. That could be a likely cause of the overstretched T96 model field in the inner magnetosphere, as already mentioned in Paper 1. Since the present work is focused on the inner and near magnetosphere, the directional criterion was abandoned here in favor of a standard fitting method, minimizing the rms deviation of the full vectors of the external field.

#### 4.2. Results

The model parameters were fitted to a subset of the new database, including only data taken sunward from  $X_{GSM} = -15 R_E$ . The fitting algorithm was based on an iterative method, used in the derivation of our earlier empirical models (see Appendix of *Tsyganenko* [1990]). The expansion coefficients were evaluated at each iteration by a standard least squares technique, and then the nonlinear parameters were obtained using the Newton-Lecam-Marquardt method. That also made it possible to estimate relative errors of the obtained values of the model parameters, as briefly outlined below.

In general, the relative importance of individual terms in a mathematical model can be evaluated by several methods. The easiest approach would be to drop a term and check the change in the merit function  $\sigma$  after re-fitting the modified model to the same dataset. Another method is to calculate mutual correlations between the model parameters, using standard algorithms of the statistical modeling theory and assuming a normal distribution of the irregular component of the modeled magnetic field. If a pair of model coefficients is highly correlated, it means that their variations cause similar changes in the model field, and, with the given dataset, it is hardly possible to accurately resolve their individual values. Under the same assumptions, it is also possible to directly evaluate the statistical uncertainties of the model parameters.

The total number of records in the data subset used in the derivation of the present model was 45,202, the average magnitude of the observed external field (i.e., after subtracting the Earth's contribution) was  $\langle \mathbf{B}_{\text{obs}}^2 \rangle^{1/2} = 33.1$  nT, and the residual rms deviation of the model field vector from the data  $\sigma = \langle [\mathbf{B}_{\text{obs}} - \mathbf{B}_{\text{mod}}]^2 \rangle^{1/2}$  was 14.0 nT, that is,  $\approx 42.3\%$  of  $\langle \mathbf{B}_{\text{obs}}^2 \rangle^{1/2}$ . The apparently large value of  $\sigma$  is not at all unusual or unexpected,

since the magnetosphere is a very dynamical system, and the high level of unpredictable fluctuations in the data is inevitable. In addition, there are instrumental errors, contributing to both magnetospheric and solar wind data, as well as errors involved in the extrapolation of the interplanetary data from the L1 point to Earth's orbit. Note also that, for comparison, the "truncated" version of T87 model [Tsyganenko, 1987] yielded the relative errors of  $\approx 47\%$  for most of the Kp-index bins. Having in mind that the T87 model was based on data taken, on the average, at larger tailward distances, we could expect still larger errors for that model (most likely, exceeding 50%) if derived from the new dataset. With this in mind, the obtained relative error of the external field 42.3% appears as a significant success. Further improvements are expected from refining the existing data and adding more new measurements in the future.

Table 1 presents the results of the model parameter computation, with the estimates of their uncertainties (in percent) in the last column. Note again that the errors were calculated assuming a normal distribution of the individual values of the observed field around those predicted by the model. However, their actual distribution is, in fact, unknown, and can be quite different from the normal one. For that reason, the values of the errors in the table should be considered only as tentative estimates, illustrating their relative accuracies. Bearing in mind other potential sources of errors (such as those resulting from inaccurate interpolation of the solar wind data from the L1 point, possible remaining bad data, etc.), one can expect the actual parameter uncertainties to exceed the ones in the table by a factor of up to 2–3.

The first 8 coefficients  $t_1^{(i)}$  and  $t_2^{(i)}$ ,  $i = 0, 1, 2, 3$ , correspond to 4 terms in each of the two modules of the tail field. Their numerical values can be used to estimate the relative contribution of the cross-tail current to the inner magnetic field and to compare the effects of different interplanetary factors. First, consider a typical quiet-time situation by assuming strictly northward IMF (and hence  $G_1 = 0$ ),  $P_d = P_{d0} = 2$  nPa, and  $Dst = 0$ , which corresponds to a corrected index  $Dst^* \approx -18.4$  nT. With these input values and the tail field parameters from Table 1, a model calculation provides the contribution from the shielded tail currents  $B_z^{(E)} \approx -22.8$  nT at Earth's location, and  $B_z^{(S)} \approx -8.5$  nT near the magnetopause subsolar point.

These values are close to a model estimate by Tsyganenko and Sibeck [1994] (see their Figure 8) and have the same order as the values obtained by Turner *et al.* [2000]. Note, however, that the estimates of Turner *et*

al. were made for stormy periods, whereas the above result corresponds to a quiet tail. For a disturbed set of input parameters, say, with  $P_d = 6$  nPa,  $Dst^* = -100$  (corresponding to  $Dst = -85$ ), solar wind speed  $V = 400$  km/s, IMF  $B_y = 0$ , and  $B_z = -5$  nT, the tail current contribution at Earth increases to a much larger value  $B_z^{(E)} \approx -62$  nT, that is, by a factor of 2.7, and the dominant role here belongs to the innermost part of the cross-tail current (within  $X \geq -15 R_E$ ), providing  $\sim 75\%$  of the net  $B_z^{(E)}$ .

Another noteworthy feature concerns the relative sensitivity of the two tail field modules to variations of the solar wind pressure  $P_d$ : as can be seen from the table, the power index  $\alpha_1 = 1.24$  of the short-scale module is much larger than  $\alpha_2 = 0.38$  of the long-scale one. However, owing to the different magnitudes of the free terms ( $t_1^{(0)} = 2.48$  against  $t_2^{(0)} = -1.17$ ), and coefficients ( $t_1^{(1)} = 0.58$  against  $t_2^{(1)} = 3.57$ ), for the commonly observed values of the pressure in the range between 2 and 10 nPa, both modules have comparable magnitudes, varying with  $P_d$  in much the same way, so that the difference appears only for very low or very high values of  $P_d$ .

As for the IMF dependence, it is interesting to note a dramatic difference between the responses of the short-scale and long-scale modules: the former has a large positive coefficient  $t_1^{(2)} = 0.32$ , while that of the latter is small and negative,  $t_2^{(2)} = -0.06$ . In other words, southward IMF intensifies only the innermost part of the cross-tail current. The same disparity was found for the coefficients of the  $Dst$ -related terms,  $t_1^{(3)} = -0.09$  and  $t_2^{(3)} = -0.01$ , which means that  $\sim 90\%$  of the tail's contribution to the  $Dst$ -index comes from its innermost part, in line with the above estimates of  $B_z^{(E)}$ .

The nonlinear variable parameters of the cross-tail current sheet included the parameters  $\Delta X_0$  and  $\Delta X_1$  in (3), defining the average position and IMF-related shift of the inner edge of the tail current (short-scale module only), average current sheet thickness at midnight meridian  $D_0$ , the hinging distance  $R_H$ , the warping amplitude  $G$ , and the parameter  $\Delta D_y$ , quantifying the rate of the current sheet widening towards the tail's flanks. For more details on the meaning of these parameters, the reader is referred to section 2.2 of Paper 1 (Eq. (2)–(14)). The average quiet-time shift  $\Delta X_0$  of the inner tail current was found equal to  $0.7 R_E$  (sunward). Somewhat surprisingly, the best-fit value of the coefficient  $\Delta X_1$  by the index  $G_2$  in (3) turned out to be negative, although quite small. It means that the current sheet is shifted slightly tailward during periods with IMF  $B_z < 0$ . However, even for a southward IMF as large as  $-10$  nT, the shift is less than  $1 R_E$ . Note also the large values of the

corresponding errors (last column), suggesting that the small tailward shift may be an artifact of overestimating the sensitivity of the tail current magnitude to the southward IMF.

The remaining tail field parameters ( $D_0$ ,  $\Delta D_y$ ,  $R_H$ , and  $G$ ) were treated as average quantities, independent of any of the model input parameters. Their best-fit values in Table 1 are close to those derived in previous data-based models.

The next 6 coefficients,  $s^{(i)}$  and  $p^{(i)}$ ,  $i = 0, 1, 2$ , correspond to the symmetrical and partial ring current components. According to (5), we have  $s = 0.71 - 0.017 Dst^* - 0.46\sqrt{P_d}$  and  $p = -0.88 - 0.03 Dst^* + 0.19\sqrt{P_d}$ . For quiet conditions, this yields rather small magnitudes for both components,  $s = 0.37$  and  $p = -0.06$ , producing a joint contribution to the field depression on the ground of  $\sim -10$  nT. That is provided almost entirely by the SRC, so that the longitudinal peak-to-peak variation does not exceed  $\sim 1$  nT. In contrast, for a disturbed situation with, say,  $P_d = 6$  nPa and  $Dst = -85$ , the ground-level depression (from the ring current only) reaches  $\sim -41$  nT and becomes strongly asymmetric, with a dusk minimum of  $-62$  nT and a dawn maximum  $-21$  nT. Another interesting thing to note is a striking predominance of the partial component over the symmetrical one during strongly disturbed periods with high values of solar wind pressure. For example, during the great storm of May 4, 1998, the solar wind proton pressure reached 24.1 nPa at 5.29 UT, and the  $Dst$  index at that time dropped down to  $-259$  nT, which corresponded to  $Dst^* = -271$  nT. For that event, the model yields  $s = 2.99$  and  $p = 8.25$ , so that the strongly asymmetric ring current produces an average ground depression of  $-100$  nT, with a duskside minimum of  $-169$  nT and dawnside maximum  $-40$  nT.

This finding agrees very well with results of the ring current particle simulations by *Liemohn et al.* [2001], who found that the PRC is the main source of the storm-time magnetic field depression on the ground, providing more than 80% of  $Dst^*$ . In our model, the predominance of the PRC during storms is due to the opposite signs of coefficients  $s^{(2)}$  and  $p^{(2)}$  in the last terms of (5). Note that originally these terms were added solely out of empirical considerations, to add more flexibility to the model. The most likely physical meaning of the unexpected different dependence of the SRC and PRC on  $P_d$  is the high sensitivity of the PRC to the particle density in the plasma sheet and hence in the solar wind. As shown by the simulations of *Liemohn et al.* [2001], the arrival of a dense magnetic cloud and the onset of enhanced convection result in a rapid buildup of ion

pressure on the duskside, which gives rise to a strong partial ring current. Since that chain of events takes a finite time, one realizes that the terms with  $\sqrt{P_d}$  in (5) should in principle use an average over the preceding hourly interval, rather than an instantaneous value. A more accurate and detailed treatment of these aspects is left for a separate future study, which will be based exclusively on stormy periods.

The nonlinear parameters of the ring current are the average scale sizes  $\xi_{s0}$  and  $\xi_{p0}$ , the power indices  $\beta_s$  and  $\beta_p$ , entering in (6), and the parameter  $Dst_0^*$ , entering in (7). Their numerical values, obtained from the data, imply that during quiet conditions the SRC is by a factor 1.3 larger than initially assumed, and its size decreases only slightly with growing  $|Dst^*|$ , indicated by the small value of the power index  $\beta_s = 0.03$ . For the PRC, the quiet-time scale size was found to be close to its initial value ( $\xi_{p0} = 0.99$ ), but the power index turned out much larger than for the SRC,  $\beta_p = 0.22$ , so that the PRC significantly shrinks onto inner L-shells with growing disturbance level. Finally, the rotation parameter  $Dst_0^*$  of the PRC was found equal to 41.6 nT; using that value, one can see from (7) that even under quiet conditions ( $Dst^* = -18.4$ ) the PRC is already rotated duskward by  $\delta \sim 37^\circ$  (although it is very weak); for  $Dst^* = -50$  the rotation angle increases to  $\delta \sim 75^\circ$ , and during strong storms with  $Dst^* \sim -150$  the PRC is centered at the dusk meridian. Note that the assumed coefficient  $\pi/2$  in (7) limits the maximal rotation angle to  $90^\circ$ . In principle, it could be replaced by a variable parameter, making possible a more detailed investigation of the PRC behavior. That question will also be addressed in a future study.

The next 8 linear parameters in Table 1 are the coefficients  $b_l^{(m0)}$  and  $b_l^{(m1)}$ , entering in (8) and defining the strength and longitudinal distribution of the model Birkeland currents. The actual expansions for the vector potential (Eq. (17) in paper 1) also included a normalization factor, such that for a given Fourier mode  $m$ , the numerical value of the corresponding coefficient  $b_l^{(m)}$  in the left-hand side of (8) was equal to the total current in MA for that mode. With that, one can see that the obtained values are in general agreement with existing estimates of Birkeland currents. For example, taking an average solar wind speed 400 km/s and IMF  $B_z = -5$  nT, so that  $G_2 = 10$ , we obtain  $b_1^{(1)} \approx 2.0$ , which corresponds to a total downward Region 1 current of 2 MA, in agreement with an estimate of *Bythrow and Potemra* [1983] (see their Fig.4). At low altitudes above the polar caps, a model current of that magnitude yields a disturbance of  $\Delta B_x \approx 350$  nT, typically observed under southward IMF conditions [e.g., *Iijima et al.*, 1982]. For northward IMF periods, the model predicts a drop of the

Region 1 current magnitude down to the quite small value 0.3 MA. The second harmonic coefficient  $b_1^{(2)}$  of the Region 1 current is significantly smaller than the first one,  $b_1^{(1)}$ , and has the same sign, suggesting a slight shift of the current peaks from the dawn-dusk meridian towards noon.

As expected, the values obtained for the coefficients  $b_2^{(10)}$  and  $b_2^{(11)}$  of the model Region 2 current are both negative, appropriate for its flow direction, opposite from the Region 1 current. The total magnitude of the Region 2 current was found to be roughly half of that for Region 1, in a good agreement with earlier data [Iijima and Potemra, 1978]. This is in contrast with the T96 model, which was unable to separately resolve the magnitude of the Region 2 current from the data, and it therefore had to be prescribed as a fixed fraction of the Region 1 current. The main reason the present effort was able to do more has been the much better data coverage of the inner polar magnetosphere. As in the case of Region 1 system, the Region 2 currents dramatically increase with the IMF-dependent parameter  $G_2$ , from 0.17MA for  $G_2 = 0$  (northward IMF) to 0.9MA for  $G_2 = 10$ . Their peaks at low altitude also shift sunward from the dawn-dusk meridian with growing IMF index  $G_2$  (that is, during periods of southward IMF), and the effect is stronger than for the Region 1 currents.

Another encouraging fact, evident from the obtained values of the nonlinear parameters  $\varsigma_1^{(0)}$ ,  $\varsigma_1^{(1)}$ ,  $\varsigma_2^{(0)}$ , and  $\varsigma_2^{(1)}$ , is an equatorward expansion of both current systems with growing parameter  $G_2$ . For the same range of the variation of  $G_2$  between 0 and 10, the diameter of the Region 1 and 2 zones increases by 12% and 27%, respectively. This agrees well with the observed statistical behavior of the Region 1 and 2 zones [Iijima and Potemra, 1978]. Note, again, that the T96 model did not reproduce the equatorward shift of the field-aligned currents.

The next two linear parameters in the Table 1 are two IMF penetration coefficients entering in (10)–(11). Their best fit values were found equal to  $\varepsilon_1 = 0.068$  and  $\varepsilon_2 = 0.554$ , which means that the penetration efficiency is strongly modulated by the IMF clock angle: while for a purely northward IMF  $\varepsilon = 0.068$ , it rises nine-fold to  $\varepsilon = 0.622$  for  $\theta = 180^\circ$ . Note in this regard that in the T96 model the interconnection field followed the direction of  $\mathbf{B}_\perp^{\text{IMF}}$ , but its magnitude, by construction, was independent of the IMF clock angle.

Finally, the last adjustable nonlinear parameter of the model was the overall scaling power index  $\kappa$ , mentioned in section 3.4. Fitting it to the data yielded a value  $\kappa = 0.158$ . This is significantly larger than

$\kappa = 0.14$  obtained in the T96 model, but still somewhat smaller than the theoretical value 0.167 of *Mead and Beard* [1964], based on a simple vacuum model with a dipole inside a pressure-balanced boundary. The discrepancy with the vacuum model can be attributed to at least three reasons. The obvious first one is the existence of magnetospheric current systems, ignored in the vacuum model. In this regard, one has to keep in mind that we assumed a self-similar scaling of dimensions of the cross-tail and Birkeland currents, proportional to the magnetopause compression and expansion. That was necessary to keep their fields confined within the magnetopause for all values of the solar wind pressure. In actuality, that assumption may be at best an approximation, which could be partially removed, for example, by including a pressure-dependent term in Eq. (4), defining the position of the inner edge of the current sheet. The second complicating factor is inevitable inaccuracy of estimating the solar wind pressure at Earth's orbit, due to instrumental errors, the large separation between WIND and Earth, foreshock effects at IMP 8, etc. A third possible source of discrepancy can be the influence of the IMF on the magnetopause shape, ignored in the present model. An investigation of the relative importance of these effects will be made in a future work.

## 5. Discussion

The foremost goal of this publication was to report initial results of the new modeling effort, confirming the feasibility of the approach and the good quality of the data, rather than to present a "final" version of the data-based model. It also provides a baseline of the average behavior of the magnetosphere during quiet and moderately disturbed times, for comparison by later studies, focused on magnetic storms and substorms.

As shown in the preceding section, the obtained values of model parameters were found in a reasonable agreement with those expected from previous observations, modeling studies, and numerical simulations. In this section we try to assess the overall accuracy of representing spacecraft data by the model, by comparing its output with the field observed at individual orbits in various regions. We will also evaluate the improvements on the T96 model and outline priorities for further research.

Plate 1 compares the external part of the magnetic field (i.e., with the IGRF field subtracted) observed by Polar on 02/09/1997 and on 08/28/1997, with the output of the present model and with that of T96. The data



of Polar are especially suitable for an overall check of the model, since the spacecraft samples both high- and low-latitude regions within the same orbit, allowing a quick glimpse of a relatively large domain. In both cases, the magnetosphere was moderately disturbed, with the  $Dst$  index varying between  $-15$  and  $-60$  nT. At middle distances and near the apogee, the difference between the two model fields is not too large. However, as the spacecraft moves into the inner magnetosphere (perigees indicated by arrows), in both cases the T96 model predicted a much more depressed field than was actually observed, which is clearly seen in the plot for  $B_z$  component. As expected, the new model yields significantly better results in that region.

To quantitatively evaluate an overall performance of both models, we used the entire modeling data set to statistically compare observed and predicted fields. Figure 9 displays scatter plots of the values of three GSM components of the observed external field, against those returned by the new model. The plots include all 45,202 data records used in the fitting of the model by least squares. The corresponding correlation coefficients  $R$  and the slopes of the best linear fit to the scatter plots are shown in the top of each panel. The largest correlation coefficient  $R = 0.92$  was found between the observed and model values of the  $B_x$  component, in part due to its large and well-ordered variation across the equatorial current sheet on the nightside. For the  $B_z$  component, the overall correlation is somewhat lower,  $R = 0.87$ , and there is a distinct increase of the data scatter around the best-fit line from positive to negative values of  $B_z$ . This indicates a worse predictability of  $B_z$  variations on the nightside, associated with substorm dipolarizations, in comparison with more accurate matching of the dayside compression and expansion of the model field in response to the variable ram pressure of the solar wind.

The worst correlation ( $R = 0.67$ ) was found between the observed and model values of  $B_y$ , which is partly due to a relatively narrow range of variation of that component. Another likely factor is the lack of the IMF  $B_y$ -related asymmetry in the adopted model of Birkeland currents, as discussed in section 2.3.3 of Paper 1. In this regard, note a conspicuous "branching" of the data points in the scatter plot for  $B_y$ : apart from the main cloud, stretched along the best-fit line, there exists a secondary vertical streak, corresponding to a portion of data with large observed  $|B_y|$ , in spite of much smaller values, predicted by the model. Most of these data points came from DE-1 observations: removing their 2299 data points from the full set (a total of 45,202 points) resulted in disappearance of most of the anomalous streak and a significant increase in the correlation coefficient for  $B_y$ .

from 0.67 to 0.74. A detailed study of the IMF  $B_y$  effects and a closer scrutiny of the DE-1 data is planned in a future study, in which a more general model of field-aligned currents will be introduced.

Figure 10 compares in the same format the output of the T96 model for the same set of data. As clearly seen, the scatter of the data around the best-fit line is significantly larger in this case, manifested in lower values of the correlation coefficients for all three components of  $\mathbf{B}$ , with the largest difference found for  $B_z$  ( $R = 0.87$  in the present model against  $R = 0.81$  in T96). Even more remarkable is the difference in the slopes, which quantify the overall deformation of the Earth's field by the magnetospheric currents. While the present model gave for all three components slopes close to 1, the T96 model yielded significantly smaller values, especially for  $B_y$  and  $B_z$  (0.76 and 0.71, respectively), which reflects a general overstretching of the inner and near field in T96, mentioned in the introduction to Paper 1.

It is interesting to compare "partial" effects of variations of different input parameters on the overall geometry of the near magnetosphere magnetic field. This is illustrated in Figure 11, showing plots of the model field lines in the noon-midnight meridian planes, corresponding to opposing values of the solar wind ram pressure  $P_d$ ,  $Dst$ -index, and IMF  $B_z$ . In the first case (varying pressure; two panels in the top), the values of  $P_d$  were chosen equal to 0.5 nPa (left) and 10 nPa (right), with  $Dst = 0$ , IMF  $B_y = B_z = 0$ , and  $G_1 = G_2 = 0$  in both cases. In the second case (varying  $Dst$ ; two panels in the center), the  $Dst$ -index was set at zero (left) and  $-100$  nT (right), with  $P_d = 2$  nPa, IMF  $B_y = B_z = 0$ , and  $G_1 = G_2 = 0$  in both plots. In the third case (varying IMF  $B_z$ ; bottom panels), we compare the effect of a strong southward IMF  $B_z = -10$  nT,  $G_1 = G_2 = 20$  (corresponding to the solar wind speed of 400 km/s) with that of a purely northward IMF  $B_z = +10$  nT with  $G_1 = G_2 = 0$ , keeping the other parameters at the same values:  $P_d = 2$  nPa,  $Dst = 0$ , and  $B_y = 0$ . It should be kept in mind that the assumed independent variations of  $Dst$  and IMF  $B_z$  in the latter two cases are very unlikely, because the  $Dst$ -index is significantly correlated with the IMF-related parameters. Nonetheless, it is of interest to compare the relative contribution of the two factors to the variations of the model field.

As seen in the first pair of plots, even though the 20-fold increase in the solar wind pressure results in a strong compression of the magnetopause, it only slightly changes the footpoint latitude of the dayside polar cusps, from  $78\text{--}79^\circ$  ( $P_d = 0.5$ ) to  $76\text{--}77^\circ$  ( $P_d = 10$ ). On the nightside, the rising pressure intensifies the

cross-tail current, which results in a moderate stretching of the field lines, so that the line crossing the equatorial plane at  $X = -13 R_E$  has its footpoint shifted in latitude from  $\approx 70^\circ$  down to  $\approx 66^\circ$ .

The effect of an isolated variation of the  $Dst$ -index from zero down to  $-100$  nT, shown in the two center panels, is (1) a pronounced stretch of field lines on the nightside, so that the footpoint of the equatorial point  $X = -13 R_E$  shifts from  $\approx 70^\circ$  to  $\approx 63.4^\circ$ , and (2) significant equatorward shift of the cusps from  $78\text{--}79^\circ$  ( $Dst = 0$ ) to  $74\text{--}75^\circ$  ( $Dst = -100$ ). Both effects are caused by an increase of the ring current and inner cross-tail current, due to large values of their regression coefficients with the  $Dst$ -index. Another effect of growing  $|Dst|$  is the duskward rotation of the PRC; it is not visible in the noon-midnight field line plots and will be demonstrated further below.

The bottom panels illustrate the effect of the IMF. It is interesting that a reversal from northward to southward IMF as large as 20 nT from peak-to-peak results in only a slight ( $\approx 1^\circ$ ) of the footpoint latitude for  $X = -13 R_E$  stretch on the nightside, but quite a dramatic equatorward excursion of the polar cusps from  $78\text{--}79^\circ$  ( $B_z = +10$  nT) to  $70\text{--}71^\circ$  ( $B_z = -10$  nT). This agrees with observed dayside "erosion" of the magnetosphere [Aubry *et al.*, 1970] and is a result of an increase of the inner cross-tail current and Birkeland currents, combined with the penetrating southward IMF. On the nightside, the increase of the tail current and the IMF penetration reduce the total field, while the growth of the Region 1 Birkeland current acts in the opposite direction (i.e., contributes a positive  $B_z$ ), nearly canceling the effect of the other sources. In contrast, on the dayside all the sources act in concert, adding a strong southward  $B_z$  and causing the observed depression of the total field at low latitudes, with the associated shift of the cusps and the global redistribution of the magnetic flux. Note that this implies a decrease of the magnetic pressure in the subsolar region and hence requires an earthward shift of the dayside magnetopause, to maintain the pressure balance. The present model does not allow the IMF-related variation of the magnetopause shape; including that effect is one of our top priorities for further modeling studies.

As noted above, in most real storm events all input parameters are largely different from their average quiet-time values. Plate 2 illustrates a storm-time configuration of the model field for the event of October 10, 1997. The color coding in both panels displays the distribution of the scalar difference  $\delta B$  between the total

magnitudes of the model field (including the Earth's contribution) and the purely dipolar field, visualizing the regions of depressed (red and yellow) and enhanced (violet, blue, and black) magnetic field. The plots were generated using input parameters for 7.30 UT of Oct. 10 with the following values: solar wind proton density  $N_p = 18.4 \text{ cc}^{-1}$ , bulk speed  $V = 493 \text{ km/s}$  (resulting in the total ram pressure of 8.7 nPa), IMF  $B_y = 0.3 \text{ nT}$ ,  $B_z = -10.9 \text{ nT}$ ,  $Dst = -128 \text{ nT}$ ,  $G_1 = 33.1$ , and  $G_2 = 28.5$ . The top panel displays the equatorial distribution of the model field, in which a strong dawn-dusk asymmetry is clearly visible, produced by the storm-time PRC. Note an inward tongue-like extension of the depression near the dusk meridian, a combined effect of the westward equatorial part of the PRC producing the crescent-shaped depression at  $R \sim 4 - 5 R_E$ , and of its field-aligned currents, responsible for the near-Earth "intrusion" of the  $\delta B$ . The bottom panel shows the corresponding meridional plot of field lines, in which the northern polar cusp footpoint was shifted to the rather low latitude of just  $67-68^\circ$  (in part due to a large negative value of the dipole tilt angle,  $\Psi = -14.2^\circ$ ), while the field lines on the nightside are extremely stretched, so that the line crossing the current sheet at  $X = -13 R_E$  has its footpoint at the unusually low latitude of  $\approx 61^\circ$  in the northern hemisphere.

## 6. Summary and Outlook

This work presented a new data-based model of the near and inner magnetosphere ( $X \geq -15 R_E$ ), derived with a recently compiled set of space magnetometer data and with new techniques presented in Paper 1. The modeling database included 5-min average data, taken by the ISTP spacecraft Polar (1996–99) and Geotail (1994–99), as well as a lesser amount of historical data from earlier missions ISEE-2 (1984–87), AMPTE/CCE (1984–88), AMPTE/IRM (1984–86), CRRES (1990–91), and DE-1 (1984–90). The magnetospheric data were tagged by 2-hour "trails" of 5-min average  $Dst$ , as well as IMF and solar wind data, taken by IMP 8 and Wind. An attempt was made to use the information on the previous conditions in the incoming solar wind, by using the lagged average indices  $G_1$  and  $G_2$  as additional driving parameters for the cross-tail and Birkeland currents.

The symmetric and partial components of the ring current are found to vary in a very different way. Under quiet conditions, the PRC is very weak in comparison with the SRC, but it dramatically intensifies and rotates into the dusk sector with growing  $Dst$ -field and the solar wind pressure. In contrast, the storm-time growth of the

SRC is relatively much less pronounced, in excellent agreement with recent particle simulations of *Liemohn et al.* [2001]. The innermost part of the cross-tail current is quite sensitive to the southward IMF, and provides  $\sim 90\%$  of the tail's contribution to the *Dst*-index, in a sharp contrast with the more distant tail current, which responds mainly to the solar wind pressure, with virtually no contribution to *Dst*. The Region 1 and 2 Birkeland currents rapidly grow in magnitude, slightly shift in local time towards noon, and expand to lower latitudes, in response to onset of southward IMF conditions. The coefficient of the IMF penetration inside the magnetosphere was found to dramatically increase with growing IMF clock angle: while quite small ( $\sim 0.1$ ) for northward IMF, it rises to  $\sim 0.6$  as the IMF turns southward.

As already noted, this paper presents the first step in an ongoing research, not a final modeling product. Based on the results of comparing the present model with the earlier T96, we expect further progress to be mostly made along the following lines. First, much improvement is expected from adding an IMF  $B_y$ -related asymmetry of the Birkeland currents, discussed in the beginning of this section and in section 2.3.3 of Paper 1. Second, much still remains to be done in taking into account the storm-time dynamics of all field sources, including the development and decay of the SRC and PRC, as well as temporal variations of the Birkeland currents responding to changes in their driving parameters. Third, a long-standing problem to be addressed is the IMF impact upon the shape of the model magnetopause.

**Acknowledgments.** The Geotail magnetic field data were kindly furnished by the Principal Investigator Susumu Kokubun; special thanks are also due to Tsugunobu Nagai, who provided me with a correction table of the Geotail magnetometer offsets, and to Don Fairfield for numerous discussions of that problem. The data of Polar were provided by Chris Russell and his team. The data of ISEE-2 were obtained from NSSDC (originally provided by Chris Russell). Processing of AMPTE/CCE data (Principal Investigator Mario Acuna) was greatly facilitated owing to the assistance and helpful advices of Peter Karlsson, Brian Anderson, and Victor Sergeev. The magnetic field data of AMPTE IRM, downloaded from the website of the University of New Hampshire (courtesy Lynn Kistler) were made available by Hermann Luhr. The CRRES magnetometer data were made available by Jeff Hughes and Howard Singer, and I am thankful to Howard for his prompt and helpful consultations on the data. The DE-1 data were retrieved online, using NSSDC's SPYCAT facility, and I extend my thanks to Toshihiko Iyemori for his very helpful comments with regard to those data, as well as for promptly

providing me with the SYM/ASY indices. The IMP 8 solar wind plasma data were obtained from the MIT Space Plasma Group website, and the rest of the interplanetary medium data were retrieved from NSSDC website using SPYCAT and CDAWEB. Special thanks are due to David Stern for his meticulous reading of the first draft of the paper and numerous helpful comments. This work is supported by NASA contract NAS5-32993 (ISTP Solarmax Extended Science Program), and NSF Magnetospheric Physics Program grant ATM-9819873.

## References

- Akasofu, S.-I., Interplanetary energy flux associated with magnetospheric substorms, *Planet. Space Sci.*, 27, 425, 1979.
- Aubry, M. P., C. T. Russell, and M. G. Kivelson, Inward motion of the magnetopause before a substorm, *J. Geophys. Res.*, 75, 7018, 1970.
- Bryant, D. A., S. M. Krimigis, and G. Haerendel, Outline of the Active Magnetospheric Particle Tracer Explorers (AMPTE) mission, *IEEE Trans. Geosci. Remote Sens.*, 23(3), 177, 1985.
- Bythrow, P. F., and T. A. Potemra, The relationship of total Birkeland currents to the merging electric field, *Geophys. Res. Lett.*, 10, 573, 1983.
- Campbell, W. H., Geomagnetic storms, the Dst ring-current myth and lognormal distribution, *J. Atm. Terr. Phys.*, 58, 1171, 1996.
- Fairfield, D. H., M. H. Acuna, L. J. Zanetti, and T. A. Potemra, The magnetic field of the equatorial magnetotail: AMPTE/CCE observations at 8.8  $R_E$ , *J. Geophys. Res.*, 92, 7432, 1987.
- Fairfield, D.H., N.A. Tsyganenko, A.V. Usmanov, M.V. Malkov, A large magnetosphere magnetic field database, *J. Geophys. Res.*, , 99, 11319, 1994.
- Fairfield, D. H., and J. Jones, Variability of the tail lobe field strength, *J. Geophys. Res.*, 101, 7785, 1996.
- Farthing, W. H., M. Sugiura, and B. G. Ledley, Magnetic field observations on DE-A and -B, *Space Sci. Instrum.*, 5, 551, 1981.
- Hilmer, R. V., and G.-H. Voigt, A magnetospheric magnetic field model with flexible current systems driven by independent physical parameters, *J. Geophys. Res.*, 100, 5613, 1995.
- Iijima, T., and T. A. Potemra, Large-scale characteristics of field-aligned currents associated with substorms, *J. Geophys. Res.*, 83, 599, 1978.
- Iijima, T., and T. A. Potemra, The relationship between interplanetary quantities and Birkeland current densities, *Geophys. Res. Lett.*, 9, 442, 1982.
- Iijima, T., N. Fukushima, and R. Fujii, Transverse and parallel geomagnetic perturbations over the polar regions observed by MAGSAT, *Geophys. Res. Lett.*, 9, 369, 1982.
- Iyemori, T., Storm-time magnetospheric currents inferred from mid-latitude geomagnetic field variations, *J. Geomagn. Geoelectr.*, 42, 1249, 1990.
- Kokubun, S., T. Yamamoto, M. H. Acuna, K. Hayashi, K. Shiokawa, and H. Kawano, The Geotail magnetic field experiment,

- J. Geomagn. Geoelectr.*, 46, 7, 1994.
- Liemohn, M. W., J. U. Kozyra, M. F. Thomsen, J. L. Roeder, G. Lu, J. E. Borovsky, and T. E. Cayton, Dominant role of the asymmetric ring current in producing the stormtime  $Dst^*$ , *J. Geophys. Res.*, 106, 10,883, 2001.
- Luhr, H., N. Klockner, W. Oelschlagel, B. Hausler, and M. H. Acuna, The IRM fluxgate magnetometer, *IEEE Trans. Geosci. Remote Sens.*, 23(3), 259, 1985.
- Mead, G.D., and Beard, D.B., Shape of the geomagnetic field – solar wind boundary, *J. Geophys. Res.*, 69, 1169, 1964.
- Mead, G. D., and D. H. Fairfield, A quantitative magnetospheric model derived from spacecraft magnetometer data, *J. Geophys. Res.*, 80, 523, 1975.
- Nakabe, S., T. Iyemori, M. Sugiura, and J. A. Slavin, A statistical study of the magnetic field structure in the inner magnetosphere, *J. Geophys. Res.*, 102, 17,571, 1997.
- Newell, P. T., D. Xi, C.-I. Meng, M. G. Kivelson, Dynamical polar cap: A unifying approach, *J. Geophys. Res.*, 102, 127, 1997.
- Nishida, A., The Geotail mission, *Geophys. Res. Lett.*, 21, 2871, 1994.
- Ogilvie, K. W., T. von Rosenvinge, and A. C. Durney, International Sun-Earth Explorer: A three-spacecraft program, *Science*, 198(4313), 131, 1977.
- Ostapenko, A. A., and Yu. P. Maltsev, Relation of the magnetic field in the magnetosphere to the geomagnetic and solar wind activity, *J. Geophys. Res.*, 102, 17,467, 1997.
- Peredo, M., D.P. Stern, and N.A. Tsyganenko, Are existing magnetospheric models excessively stretched ?, *J. Geophys. Res.*, 98, 15343, 1993.
- Potemra, T. A., L. J. Zanetti, and M. H. Acuna, The AMPTE CCE magnetic field experiment, *IEEE Trans. Geosci. Remote Sens.*, 23(3), 246, 1985.
- Richardson, J. D., and K. I. Paularena, Plasma and magnetic field correlations in the solar wind, *J. Geophys. Res.*, 106, 239, 2001.
- Russell, C. T., The ISEE 1 and 2 fluxgate magnetometers, *IEEE Trans. Geosci. Remote Sens.*, 16(3), 239, 1978.
- Russell, C. T., R. C. Snare, J. D. Means, D. Pierce, D. Dearborn, M. Larson, G. Barr, and G. Le, The GGS/Polar magnetic fields investigation, *Space Sci. Rev.*, 71, 563, 1995.
- Singer, H. J., W.P. Sullivan, P. Anderson, F. S. Mozer, P. Harvey, J. R. Wygant, W. McNeil, Fluxgate Magnetometer Instrument on the CRRES, *Journ. Spacecraft and Rockets*, 29(4), 599, 1992.



- Tsyganenko, N.A., Global quantitative models of the geomagnetic field in the cislunar magnetosphere for different disturbance levels, *Planet.Space Sci.*, 35, 1347, 1987.
- Tsyganenko, N.A., A magnetospheric magnetic field model with a warped tail current sheet, *Planet.Space Sci.*, 37, 5, 1989.
- Tsyganenko, N. A., Quantitative models of the magnetospheric magnetic field: Methods and results, *Space Sci. Rev.*, 54, 75, 1990.
- Tsyganenko, N. A., Solar wind control of the tail lobe magnetic field as deduced from Geotail, AMPTE/IRM, and ISEE-2 data, *J. Geophys. Res.*, 105, 5517, 2000a.
- Tsyganenko, N. A., Recent progress in the data-based modeling of magnetospheric currents, in *Magnetospheric Current Systems, Geophysical Monograph Ser.*, v.118, edited by S.-I. Ohtani, R.-I. Fujii, R. Lysak, and M. Hesse, p.61, AGU, Washington, D. C., 2000b.
- Tsyganenko, N. A., A model of the near magnetosphere with a dawn-dusk asymmetry 1. Mathematical structure, a companion paper, *J. Geophys. Res.*, this issue, 2001.
- Tsyganenko, N. A., and A. V. Usmanov, Determination of the magnetospheric current system parameters and development of experimental geomagnetic field models based on data from IMP and HEOS satellites, *Planet. Space Sci.*, 30, 985, 1982.
- Tsyganenko, N. A., and D. G. Sibeck, Concerning flux erosion from the dayside magnetosphere, *J. Geophys. Res.*, 99, 13,425, 1994.
- Tsyganenko, N. A., S. B. P. Karlsson, S. Kokubun, T. Yamamoto, A. J. Lazarus, K. W. Ogilvie, C. T. Russell, Global configuration of the magnetotail current sheet as derived from Geotail, Wind, IMP 8 and ISEE 1/2 data, *J. Geophys. Res.*, 103, 6827, 1998.
- Tsyganenko, N. A., G. Le, C. T. Russell, and T. Iyemori, A study of the inner magnetosphere based on data of Polar, *J. Geophys. Res.*, 104, 10,275, 1999.
- Turner, N. E., D. N. Baker, T. I. Pulkkinen, and R. L. McPherron, Evaluation of the tail current contribution to *Dst*, *J. Geophys. Res.*, 105, 5431, 2000.
- Wygant, J. R., R. B. Torbert, and F. S. Mozer, Comparison of S3-3 polar cap potential drops with the interplanetary magnetic field and models of magnetopause reconnection, *J. Geophys. Res.*, 88, 5727, 1983.

---

N. A. Tsyganenko, USRA, Code 690.2, Laboratory for Extraterrestrial Physics, NASA Goddard Space Flight Center, Greenbelt, MD 20771. (kolya@nssdca.gsfc.nasa.gov)

Received ... , 2001; revised ....., 2001; accepted ....., 2001.

Submitted to the *Journal of Geophysical Research*, 2001.

**Figure 1.** Numbers of data records and covered time periods are shown here for various spacecraft, contributed to the modeling data set. Thickness of the bars is proportional to the square root of the number of the data records per year. The total contributions (numbers of 5-min records with complete 2-hour solar wind data trails) from each spacecraft are given in parentheses after their names.

**Figure 2.** Variation of the Geotail  $B_z$  offset over the entire period 1994–1999, covered by the modeling data set. The tabular data (courtesy T. Nagai) are shown by crosses, and the solid line is an analytical approximation used in the data processing.

**Figure 3.** Views of the equatorial (left) and noon-midnight projections of the spatial coverage by the Geotail data of the modeling region. Each point represents a 5-min average data record. See Figure 1 for the temporal coverage and the total number of data records.

**Figure 4.** Same as Figure 3 but showing the data of Polar.

**Figure 5.** Same as Figure 4 but showing the data of ISEE-2 (triangles) and AMPTE/IRM (squares).

**Figure 6.** Same as Figure 5 but showing the data of AMPTE/CCE.

**Figure 7.** Same as Figure 6 but showing the data of CRRES.

**Figure 8.** Same as Figure 7 but showing the data of DE-1.

**Figure 9.** Scatter plots of the observed GSM components of the external part of the total geomagnetic field against those returned by the present model.

**Figure 10.** Same as Figure 9, but for the T96 model.

**Figure 11.** Illustrating the effects of changing individual input parameters of the model in the noon-midnight configuration of the geomagnetic field lines: (top) solar wind ram pressure, (center)  $Dst$ -index, and (bottom) IMF  $B_z$ . The field lines have been plotted at 1-degree intervals of the footpoint latitude  $\lambda$ ; highlighted are those starting at  $\lambda = 60^\circ, 65^\circ, 70^\circ, \dots, 85^\circ, 90^\circ$ .

**Plate 1.** Two daily plots of the GSM magnetic field components of the external magnetic field (i.e., without Earth's contribution). Three traces in each panel correspond to the field measured by Polar (black dots), returned by T96 model (red), and by the present one (blue). The upper three panels compare the model output with the observations made on Feb. 9, 1997, and the lower ones are for Aug. 28, 1997. Note a large overestimate of  $|B_z|$  by T96 near the perigees (indicated by vertical arrows).

**Plate 2.** Spatial distribution of the difference  $\delta B$  between the magnitudes of the total model field and the purely dipolar one, for a strong storm event of October 10, 1990. The plots correspond to 7.30 UT, when the solar wind pressure equaled 8.7 nPa,  $Dst = -128$  nT, IMF  $B_y = 0.3$  nT,  $B_z = -10.9$  nT, and the dipole tilt angle  $\Psi = -14.2^\circ$ . The top panel shows a near-equatorial distribution of  $\delta B$ , calculated over a surface, nearly corresponding to the surface of minimum  $B$  in the center of the warped cross-tail current sheet on the nightside. Note a significant duskward rotation of the field depression in the inner magnetosphere as well as the earthward extension of the depressed region near dusk, caused by the magnetic effect of field-aligned closure currents associated with the PRC. The bottom panel also shows the noon-midnight configuration of the model field lines, traced with a 1-degree interval of the footpoint latitude, starting from  $59^\circ$  of geomagnetic latitude in the northern hemisphere.

**Table 1.** Parameters of the Model Field Sources, Entering in (2)–(3) and (5)–(11)

Parameter	Value	Error (%)
<i>Coefficients</i>		
$t_1^{(0)}$	2.483	5.2
$t_1^{(1)}$	0.583	13.1
$t_1^{(2)}$	0.319	3.6
$t_1^{(3)}$	-0.088	4.1
$t_2^{(0)}$	-1.173	36.4
$t_2^{(1)}$	3.575	11.8
$t_3^{(2)}$	-0.061	11.9
$t_4^{(3)}$	-0.011	15.4
$s^{(0)}$	0.709	2.8
$s^{(1)}$	-0.0168	2.5
$s^{(2)}$	-0.461	2.7
$p^{(0)}$	-0.878	6.4
$p^{(1)}$	-0.030	3.8
$p^{(2)}$	0.189	17.0
$b_1^{(10)}$	0.281	3.6
$b_1^{(11)}$	0.166	1.5
$b_1^{(20)}$	-0.029	17.9
$b_1^{(21)}$	0.026	4.8

**Table 1.** (continued)

Parameter	Value	Error (%)
$b_2^{(10)}$	-0.236	4.8
$b_2^{(11)}$	-0.077	3.1
$b_2^{(20)}$	0.091	5.8
$b_2^{(21)}$	-0.025	4.7
$\varepsilon_1$	0.068	24.7
$\varepsilon_2$	0.554	5.5
<i>Nonlinear parameters</i>		
$\alpha_1$	1.244	4.6
$\alpha_2$	0.380	10.1
$\Delta X_0$	0.689	7.2
$\Delta X_1$	-0.046	9.5
$D_0$	2.36	1.1
$R_H$	8.94	0.5
$G$	28.3	1.3
$\Delta D_y$	3.900	2.6
$\xi_{S\,0}$	1.29	0.7
$\beta_S$	0.031	29.2
$\xi_{P\,0}$	0.99	1.2
$\beta_P$	0.22	4.3

**Table 1.** (continued)

Parameter	Value	Error (%)
$Dst_0^*$	41.6	7.0
$\varsigma_1^{(0)}$	1.13	0.6
$\varsigma_1^{(1)}$	0.014	3.8
$\varsigma_2^{(0)}$	1.03	1.1
$\varsigma_2^{(1)}$	0.030	5.4
$\kappa$	0.158	0.5

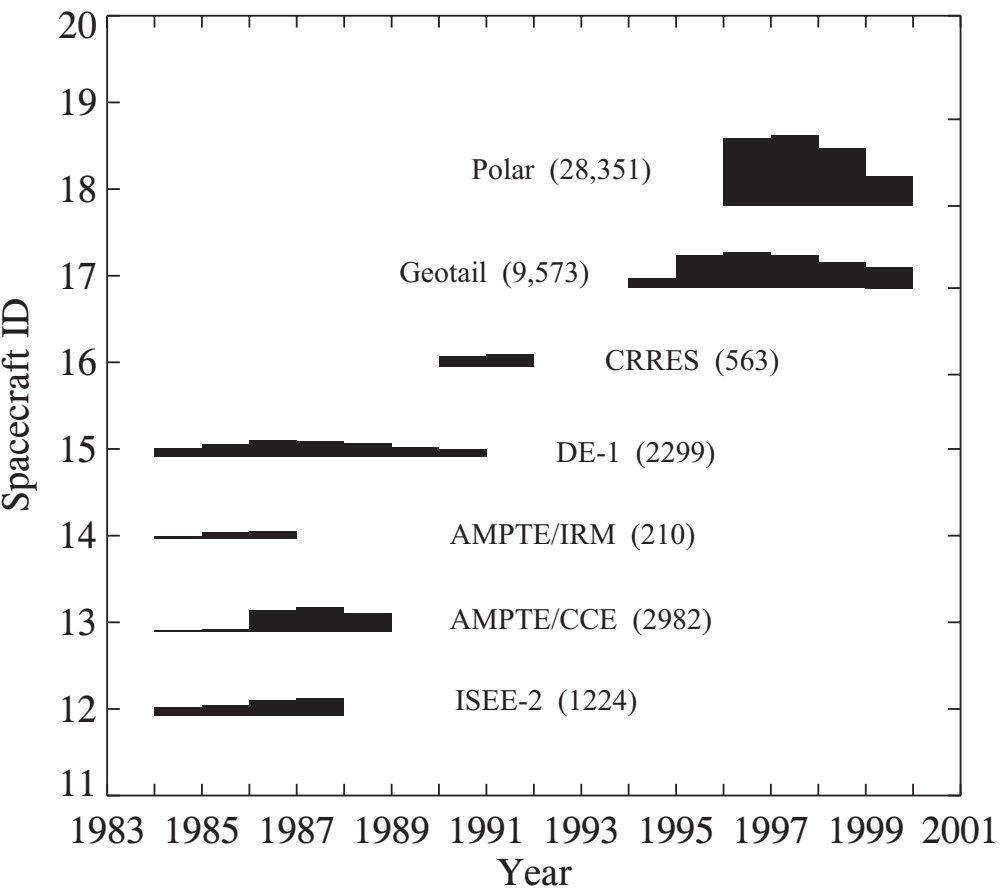


Figure 1



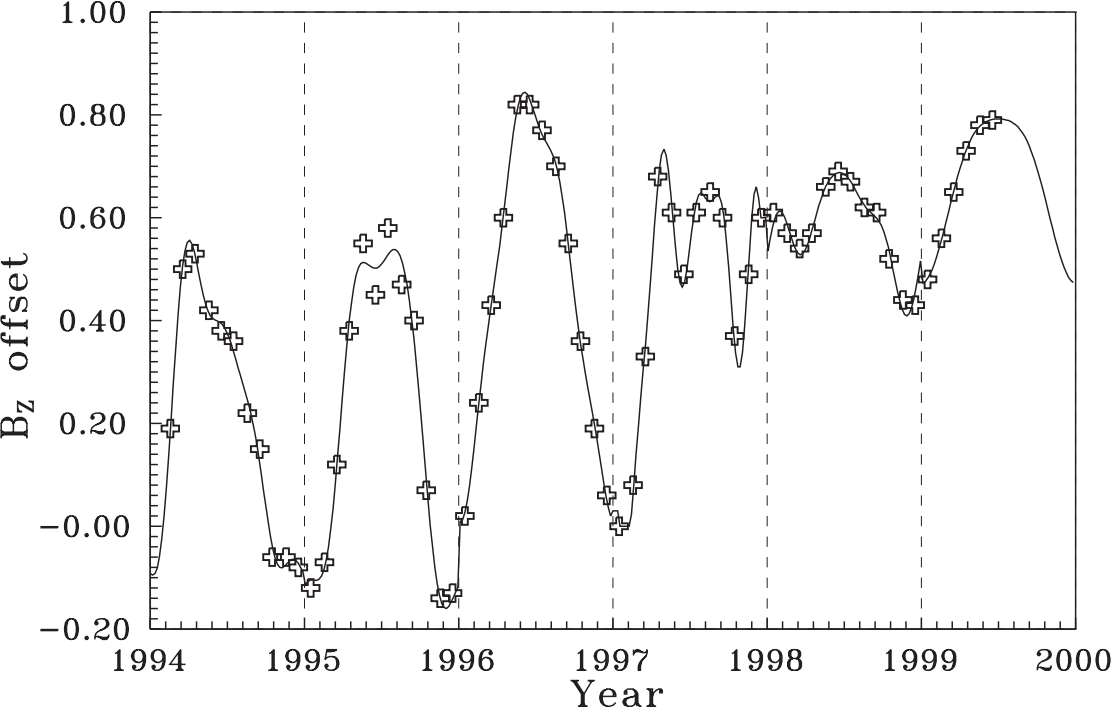


Figure 2

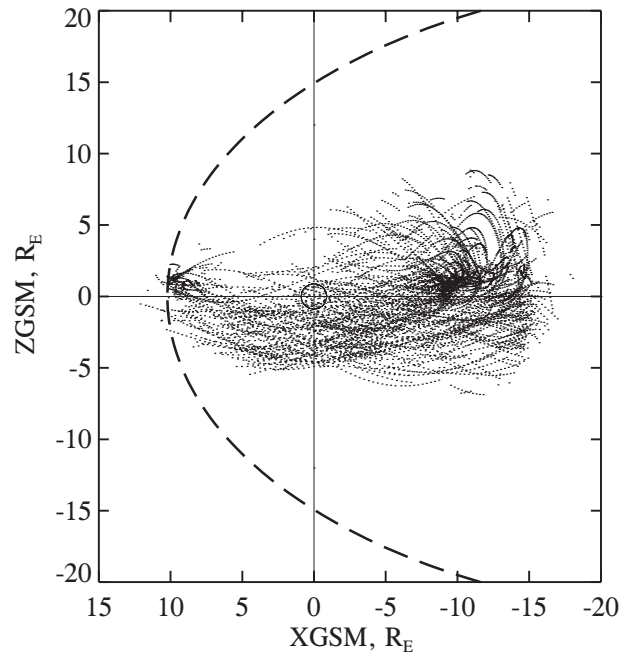
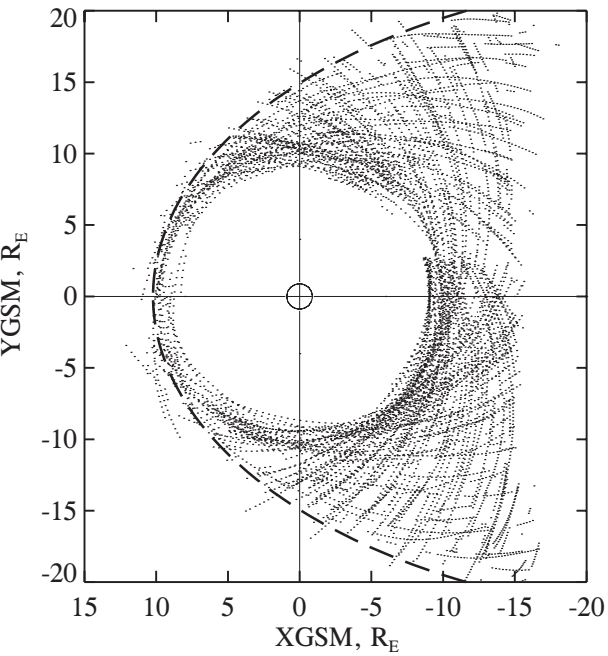


Figure 3

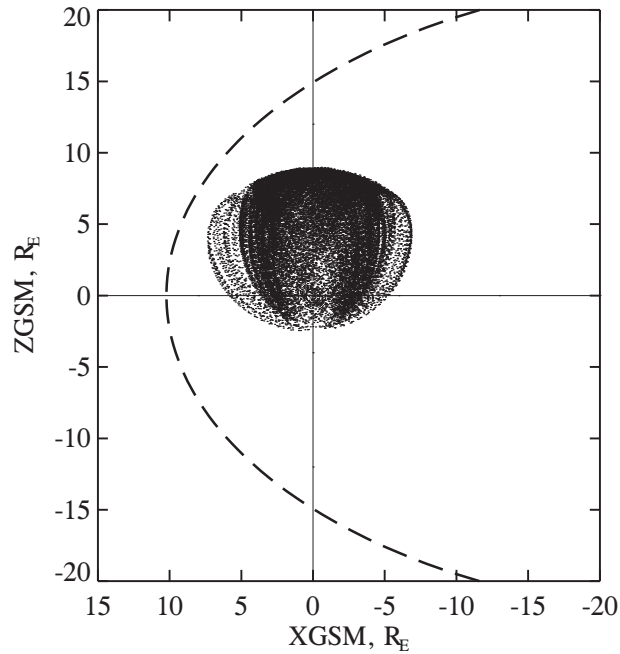
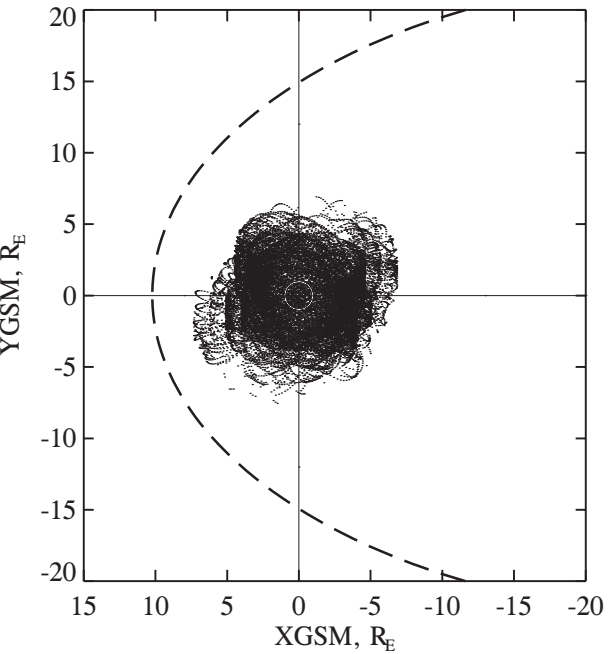


Figure 4

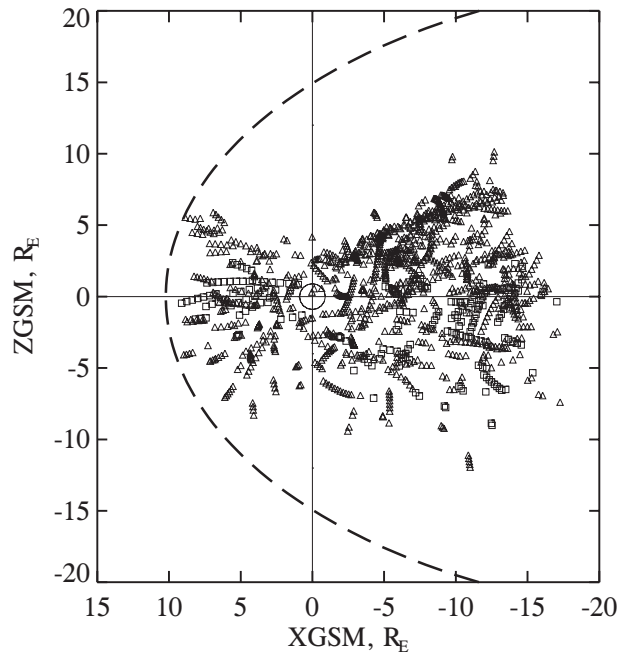
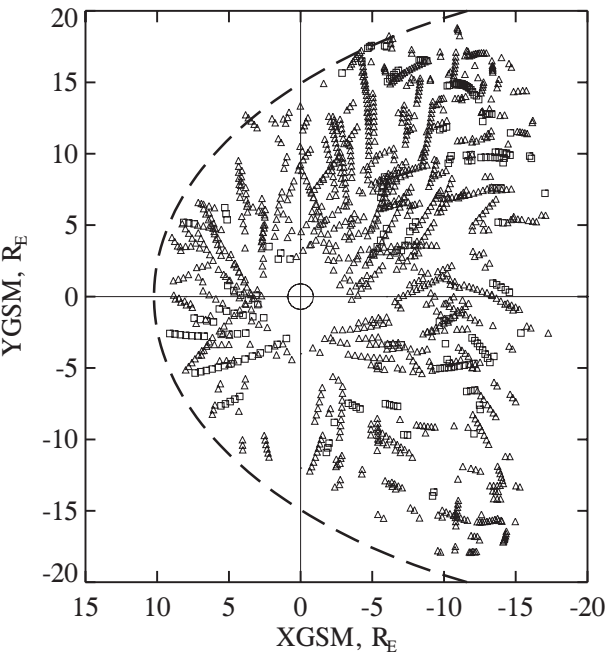


Figure 5

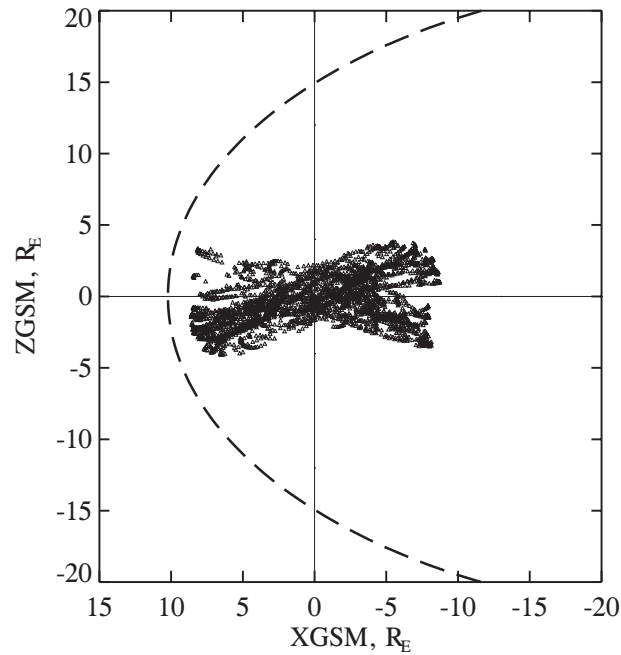
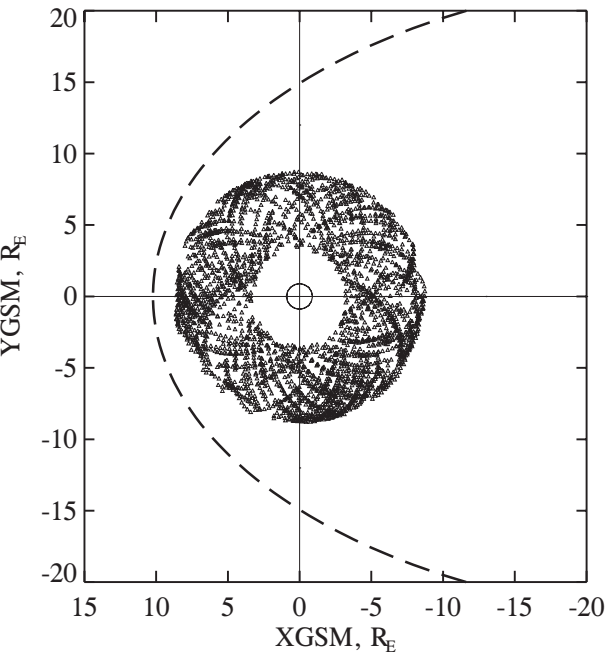


Figure 6

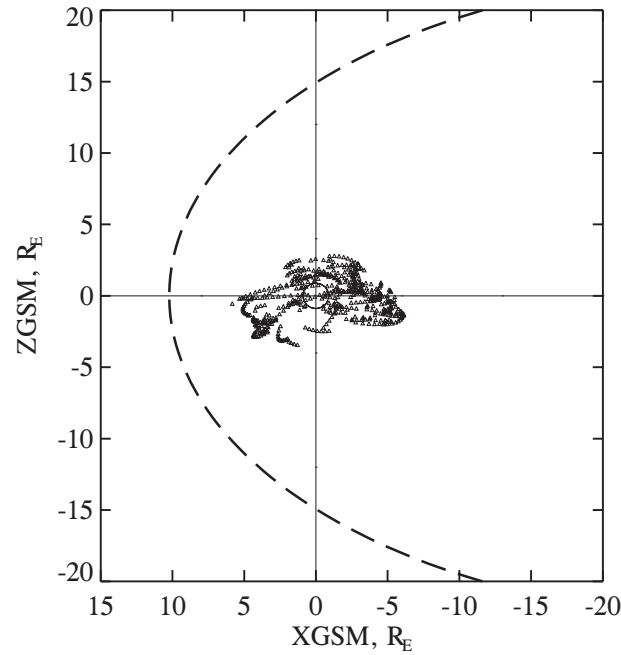
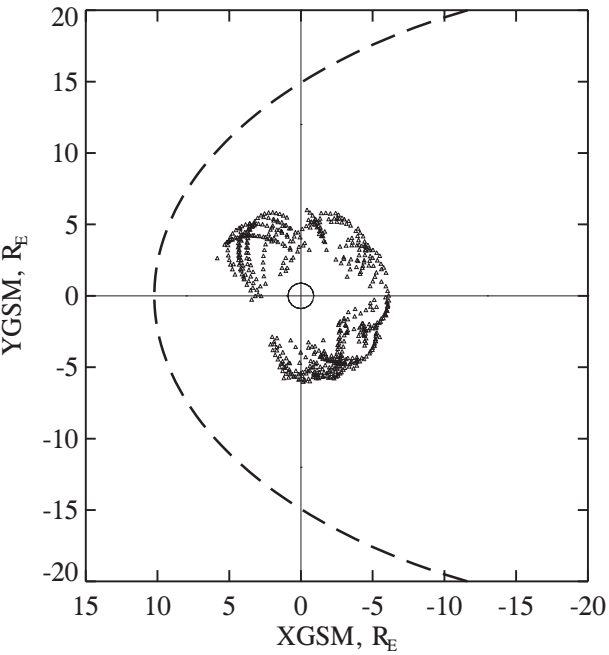


Figure 7

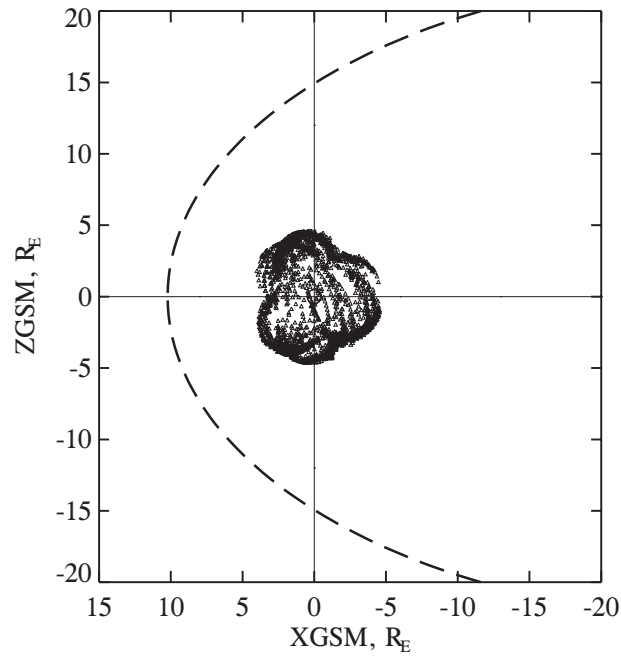
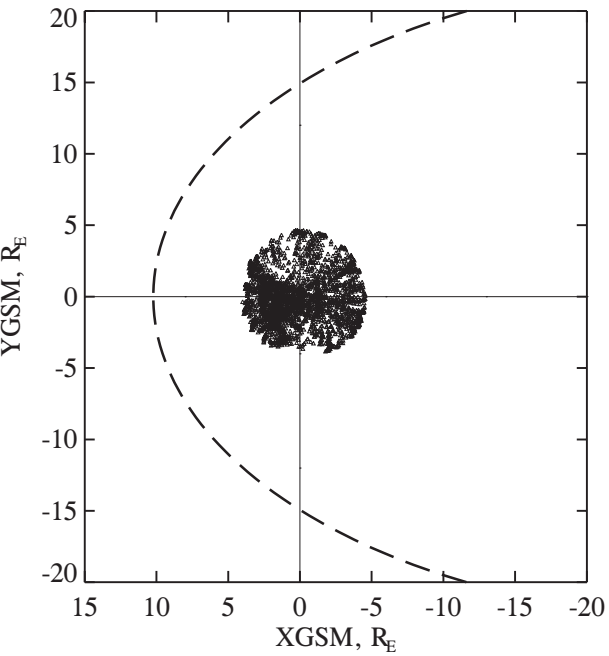


Figure 8

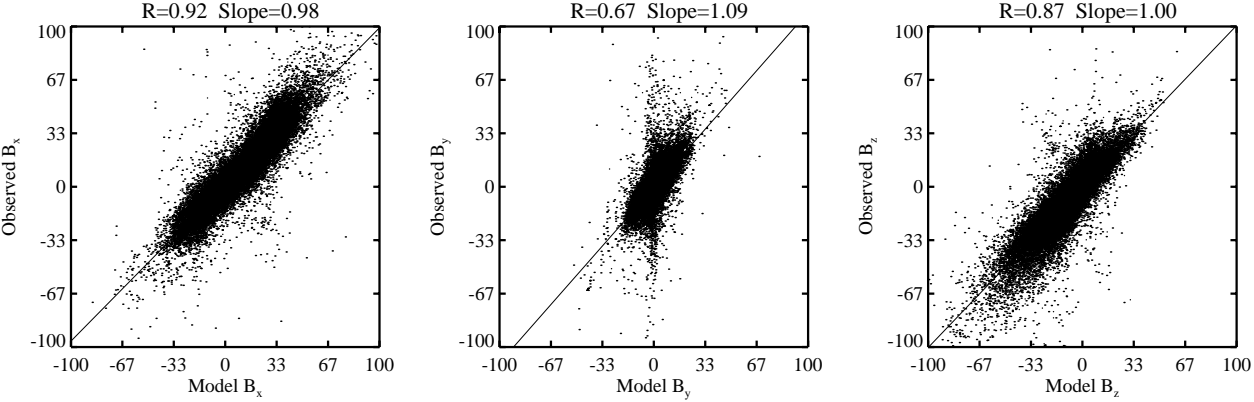


Figure 9



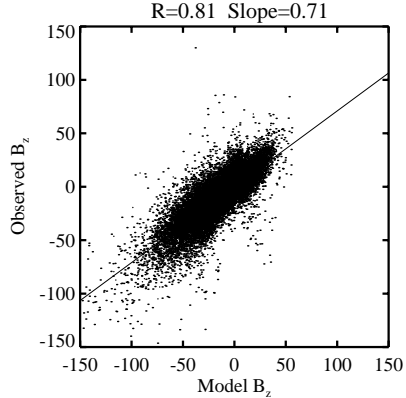
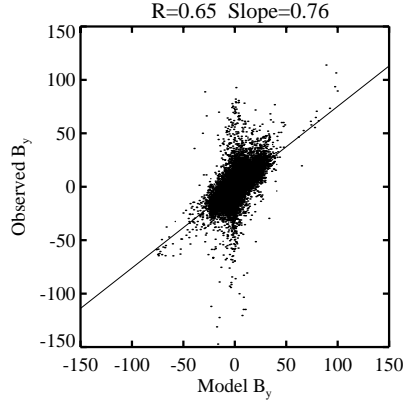
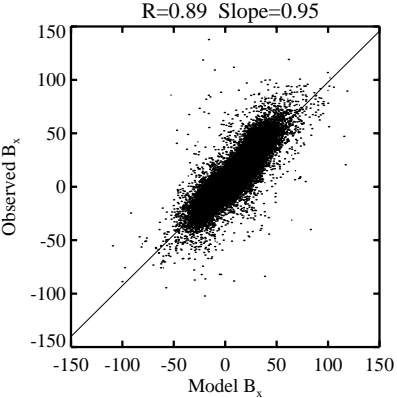


Figure 10

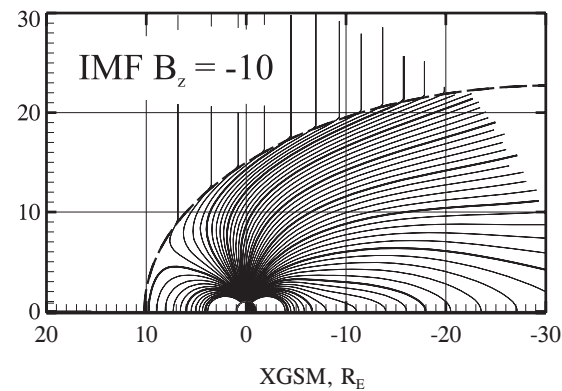
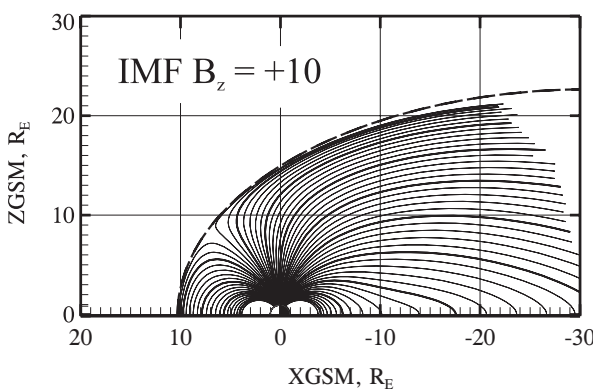
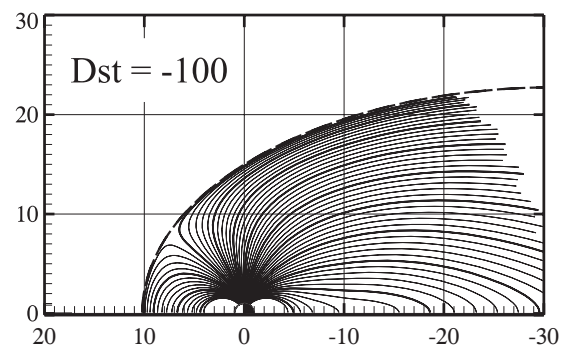
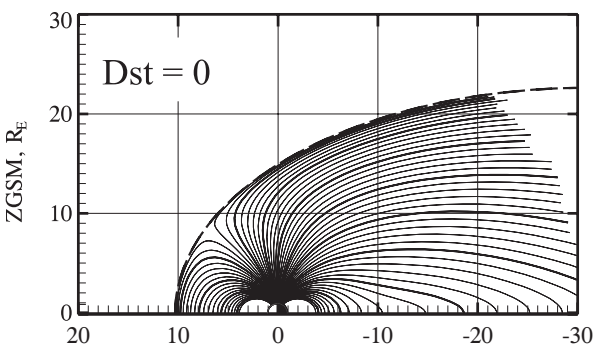
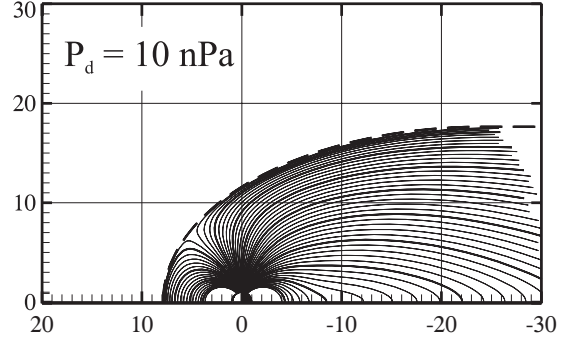
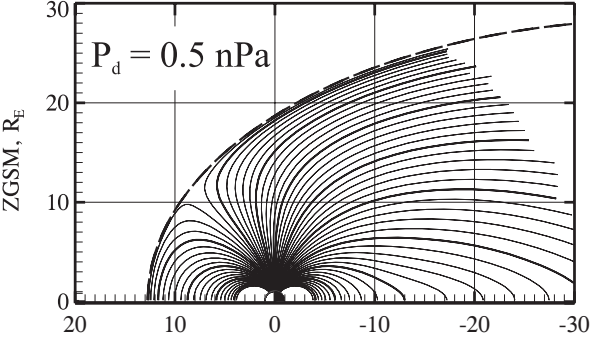


Figure 11

